The Astrophysical Journal Letters, 990:L9 (15pp), 2025 September 1 https://doi.org/10.3847/2041-8213/adf7a5

Wide Separation Planets in Time (WISPIT): Discovery of a Gap Hα Protoplanet WISPIT 2b with MagAO-X

Laird M. Close[1], Richelle F. van Capelleveen[2], Gabriel Weible[1], Kevin Wagner[1], Sebastiaan Y. Haffert[1,2], Jared R. Males[1], Ilya Ilyin[3], Matthew A. Kenworthy[2], Jialin Li[1], Joseph D. Long[4], Steve Ertel[1,5], Christian Ginski[6], Alycia J. Weinberger[7], Kate Follette[8], Joshua Liberman[9], Katie Twitchell[9], Parker Johnson[1], Jay Kueny[9], Daniel Apai[1], Rene Doyon[10], Warren Foster[1], Victor Gasho[1], Kyle Van Gorkom[1], Olivier Guyon[1,9,11,12], Maggie Y. Kautz[1], Avalon McLeod[13], Eden McEwen[9], Logan Pearce[14], Lauren Schatz[15], Alexander D. Hedglen[16], Ya-Lin Wu[17], Jacob Isbell[5], Jenny Power[5], Jared Carlson[5], Emmeline Close[18], Elena Tonucci[2], and Matthijs Mars[2]
[1] Center for Astronomical Adaptive Optics, Department of Astronomy, University of Arizona, 933 N. Cherry Avenue, Tucson, AZ 85718, USA; lclose@arizona.edu
[2] Leiden Observatory, Leiden University, PO Box 9513, 2300 RA Leiden, The Netherlands
[3] Leibniz Institute for Astrophysics Potsdam (LIAP), An d. Sternwarte 16, 14482 Potsdam, Germany
[4] Center for Computational Astrophysics, Flatiron Institute, 162 5th Avenue, New York, NY, USA
[5] LBT org, Steward Observatory, University of Arizona, USA
[6] School of Natural Sciences, Center for Astronomy, University of Galway, Galway, H91 CF50, Ireland
[7] The Earth and Planets Laboratory (EPL), Carnegie Institution for Science, USA
[8] Amherst College Department of Physics and Astronomy, Science Center, 25 East Drive, Amherst, MA, USA
[9] Wyant College of Optical Sciences, The University of Arizona, 1630 E University Boulevard, Tucson, AZ, USA
[10] University of Montreal, Montreal Quebec, Canada
[11] Subaru Telescope, National Observatory of Japan, NINS, 650 N. A'ohoku Place, Hilo, HI, USA
[12] Astrobiology Center, National Institutes of Natural Sciences, 2-21-1 Osawa, Mitaka, Tokyo, Japan
[13] Draper Laboratory, 555 Technology Square, Cambridge, MA, USA
[14] Department of Astronomy, University of Michigan, 323 West Hall, 1085 S University Ave, Ann Arbor, MI 48109, USA
[15] Starfire Optical Range, Kirtland Air Force Base, Albuquerque, NM, USA
[16] Northrop Grumman in Rolling Meadows, IL, USA
[17] Department of Physics, National Taiwan Normal University, Taipei 116, Taiwan
[18] College of Arts and Sciences, Queen's University, Canada
Received 2025 July 3; revised 2025 July 28; accepted 2025 August 2; published 2025 August 26

Abstract

Excellent (<25 mas) Hα images of the star TYC 5709-354-1 led to the discovery of a rare Hα protoplanet. This star was discovered by the WISPIT survey to have a large multi-ring transitional disk, and is hereafter WISPIT 2. Our Hα images of 2025 April 13 and 16 discovered an accreting (Hα in emission) protoplanet: WISPIT 2b ($r = 309.43 \pm 1.56$ mas; ($\sim$54 au deprojected), PA $= 242\overset{\circ}{.}21 \pm 0\overset{\circ}{.}41$) likely clearing a dust-free gap between the two brightest dust rings in the transitional disk. Our signal-to-noise ratio of 12.5 detection gave an Hα ASDI contrast of $(6.5 \pm 0.5) \times 10^{-4}$ and an Hα line flux of $(1.29 \pm 0.28) \times 10^{-15}$ erg s^{-1} cm^{-2}. We also present L' photometry from LBT/LMIRcam of the planet ($L' = 15.30 \pm 0.05$ mag), which, when coupled with an age of $5.1^{+2.4}_{-1.3}$ Myr, yields a planet mass estimate of $5.3 \pm 1.0\ M_{\rm jup}$ from the DUSTY evolutionary models. WISPIT 2b is accreting at $2.25^{+3.75}_{-0.17} \times 10^{-12}\ M_{\rm Sun}\ {\rm yr}^{-1}$. WISPIT 2b is very similar to the other Hα protoplanets in terms of mass, age, flux, and accretion rate. The inclination of the system ($i = 44°$) is also, surprisingly, very similar to the other known Hα protoplanet systems, which all cluster from $37° \leqslant i \leqslant 52°$. We argue this clustering has only a $\sim$1.0% (2.6σ) probability of occurring randomly, and so we speculate that magnetospherical accretion might have a preferred inclination range ($\sim$37°–52°) for the direct (cloud free, low extinction) line of sight to the Hα line formation/shock region. We also find at 110 mas ($\sim$15 au deprojected) a close companion candidate (CC1) that may be consistent with an inner dusty $9 \pm 4\ M_{\rm jup}$ planet.

Unified Astronomy Thesaurus concepts: Exoplanet astronomy (486); Exoplanet formation (492); Protoplanetary disks (1300); Adaptive optics (2281); Planet formation (1241); Accretion (14); T Tauri stars (1681); Exoplanet atmospheres (487)

1. Introduction

It is now well established that some gas giant protoplanets pass through a period of high luminosity as they accrete hydrogen gas from their circumplanetary disks (CPDs) producing detectable Hα emission. This was most clearly demonstrated initially in the discovery of Hα emission from PDS 70 b (K. Wagner et al. 2018), and PDS 70 c (S. Y. Haffert et al. 2019). Direct observations of protoplanets (defined here as accreting planets) are a key window into this very poorly understood process of planet formation and accretion from a CPD, which itself is embedded in a larger circumstellar disk, or transitional disk (C. Espaillat et al. 2011; L. Francis & N. van der Marel 2020). While the exact mechanisms of planetary accretion are not yet fully understood, massive planets could magnetospherically accrete, via magnetic fields, directly onto a latitude line of the planet (Z. Zhu et al. 2016; T. Thanathibodee et al. 2019; G.-D. Marleau et al. 2022, and references within). Accretion through shocks onto the CPD is also possible (J. Szulágyi & C. Mordasini 2017;

Y. Aoyama et al. 2018; Y. Aoyama et al. 2021; J. Szulágyi et al. 2022, and references within), and it is unclear which process, or a combination of both, dominate. To be clear, the Aoyama model and magnetospheric accretion model are not mutually exclusive. The Aoyama model could also explain the Hα emission in a magnetospheric accretion scenario. The difference is the origin of the emission. The Thanathibodee model assumes emission from the accretion flow tracing the magnetic field. The Aoyama model assumes emission from the shock itself. Variability studies may be able to inform which of these models are more likely (D. Demars et al. 2023; L. M. Close et al. 2025; Y. Zhou et al. 2025, and references within). The key to informing our accreting protoplanet models is to discover more systems—because there is only one really well-studied system (PDS 70) to date (L. M. Close et al. 2025, and references within). Indeed, the study of protoplanets is critical if we are to understand the process of planet formation, accretion, satellite/moon growth, CPDs, and the impact that these planets have on their host disks (clearing gaps, creating cavities, etc).

In Section 2 of this Letter, we briefly introduce the current state of Hα protoplanet detections, instrumentation, and techniques. We introduce the newly discovered transitional disk star WISPIT 2 at the end of that section. Note that our companion Letter (R. F. van Capelleveen et al. 2025; hereafter Letter 1) covers the H+Ks characterization and discovery of the star's impressive multi-ringed transitional disk and planet in the near-IR (NIR). In Section 3, we describe our MagAO-X and LBTI/LMIRcam observations of WISPIT2. In Section 4, we introduce the discovery Hα images of the protoplanet WISPIT 2b, and follow-up images at L′. Section 5 presents the Hα and L′ photometry and astrometry of WISPIT 2b. In Section 6, we analyze the Hα photometry to derive the line flux and mass accretion rate of WISPIT 2b. In Section 7, we derive a mass for WISPIT 2b from the L′ photometry, and compare to the H+Ks planetary mass from Letter 1. We also discuss WISPIT 2b compared to the other known Hα protoplanets—defined as exoplanets that have a signal-to-noise ratio (SNR) > 5 Hα emission detections at multiple epochs. At the end of this discussion, we describe an inner close companion (CC1), which could be an inner planet or an unusually red compact dust clump. Our conclusions are given in Section 8.

2. MagAO-X Instrumental Configuration for Hα Imaging

2.1. Introduction to Hα Protoplanet Imaging

It is not trivial to detect protoplanets. The only way to guarantee an actively accreting protoplanet is being detected is to directly detect accretion tracers. Using the MagAO (the predecessor AO system to MagAO-X) system, L. M. Close et al. (2014) used the strongest visible tracer of accretion (Hα) to detect the low-mass companion HD 142527 B inside the large transitional disk dust-free gap of HD 142527 A. The work of L. M. Close et al. (2014) first speculated that for low-mass ($0.5 < M_{\mathrm{p}} < 10\ M_{\mathrm{jup}}$) planets, H$\alpha$ angular spectral differential imaging (ASDI) could be a powerful tool for detection of protoplanets, particularly at the lower-mass end where Hα could be brighter than the NIR emission for active accretion. Indeed, using MagAO's SDI+ mode (L. M. Close et al. 2018), we discovered Hα emission from the PDS 70 b protoplanet (M. Keppler et al. 2018) in 2018 May (K. Wagner et al. 2018). Then, the Very Large Telescope (VLT)/MUSE discovered PDS 70 c at Hα (S. Y. Haffert et al. 2019). Recently L. M. Close et al. (2025) utilized the much improved MagAO-X SDI mode to capture PDS 70 b and c over 3 yr, showing great sensitivity to variable Hα emission from protoplanets.

2.2. New Hα Detection Techniques with Extreme Visible AO: MagAO-X

Past "Hα AO" detections were executed with older AO systems (e.g., VLT/SPHERE, VLT/MUSE, Magellan/MagAO) with relatively low (<1%–10%) Strehls at Hα. However, we have now fully commissioned the world's newest extreme AO system MagAO-X. MagAO-X is unique—it was designed from the start to work in the visible at high Strehl (J. R. Males et al. 2018, 2024). The optical design for MagAO-X is complex in that, being a woofer-tweeter system, requires two reimaged pupils, and a lower coronagraphic bench that requires another pre-apodizer pupil followed by a Lyot pupil plane. Hence, MagAO-X has four reimaged pupils created by eight off-axis parabolas (OAPs). This complex optical train could lead to thermal alignment drift and variable non-common path (NCP) errors—but each OAP is potted in our (L. Close & M. Kautz) patented ultrastable "set-and-forget" mounts (US Patent Number 11,846,828), which minimizes NCP thermal drift. MagAO-X has an $6 \times 6''$ field of view at f/69 with $0\farcs00593 \pm 0\farcs00003$ pix^{-1} platescale (with 13 μm EMCCD pixels) that yields a nicely oversampled 3.4 pix/(λ/D) at Hα. See L. M. Close et al. (2018, 2025) for more details about the optical design of MagAO-X.

MagAO-X yields a superior level of wave front control with a 2040 actuator Tweeter deformable mirror (DM) and a unique "extra" DM to eliminate all NCP errors between the science and wave front sensing (WFS) channels, minimizing coronagraphic leak (we call this DM the NCPC DM). This NCPC DM was upgraded to 1024 actuators in 2024, which greatly improved our ability to use Focal Diversity Phase Retrieval (FDPR; K. Van Gorkom et al. 2021; J. Kueny et al. 2024) to eliminate NCP errors by an artificial source NCP closed-loop calibration/elimination at the start of the night (or after a major beamsplitter change during the night). This approach is our field-tested optimal procedure to minimize NCP errors and achieve uniquely high Hα AO Strehls on faint targets.

On this run, we FDPR calibrated away NCP errors with the NCPC DM to enable ∼90%–94% Strehl (no atmospheric turbulence) at Hα on our science cameras with our "always ready" artificial source (a super-continuum laser) before the start of science operations and/or after a major beamsplitter change. It is typically only done once a night, and only takes ⩽20 minutes usually after sunset in twilight with dome fully open near (±2C) our observing temperature. After this, the artificial source is removed from the beam and the NCPC DM stays in this calibrated DM shape for the rest of the Hα imaging night and so the f/69 focus and NCPC wave front are fixed—and no more observing time is lost to any other calibrations all night long.

WFS with MagAO-X's very low noise (<0.6 rms e-readnoise) EMCCD pyramid WFS OCAM2 detector allows Strehls of >60% to be obtained at z' (908 nm; $\Delta\lambda = 130$ nm) and closed loop at 2 kHz (residual WFE <120 nm rms) with 1564 corrected modes—as demonstrated on-sky (J. R. Males et al. 2022, 2024). The low noise of this WFS sensor enables

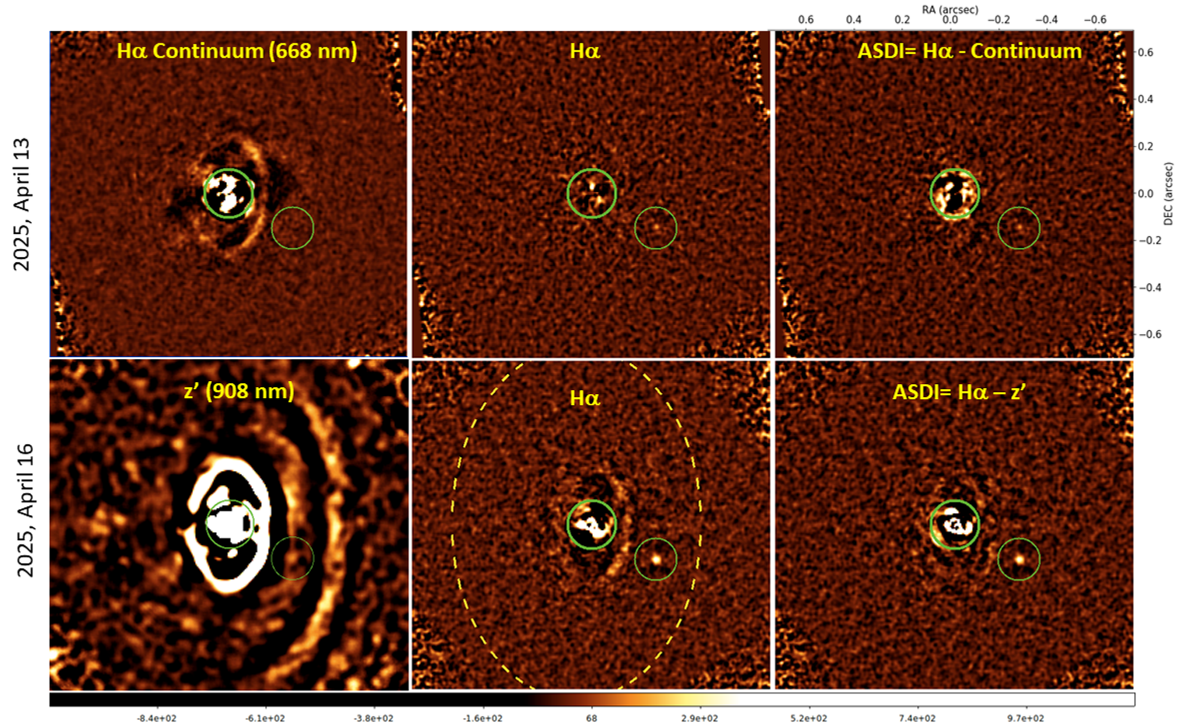

Figure 1. The discovery images of WISPIT 2b. These are both the 2025 April MagAO-X Hα pyKLIP pipeline reduced data sets. The thick central green circles (r = 103 mas) are centered on the star. The lighter-green circles (r = 89 mas) all have identical centers at WISPIT 2b (star–planet separation = 309.43 mas, PA = 242$^{\circ}_{.}$2). In the discovery image, WISPIT 2b is detected in the ASDI image at a signal-to-noise ratio (SNR) = 5.5 (top right), on April 16 it was recovered at SNR = 12.5 (bottom right). The dashed yellow line in the Hα image traces the second-brightest ring (visible at z'; called ring #2; the brightest inner ring is ring #3; see Letter 1 for ring images and names). All images have the first 5 principal component (PC) modes removed by pyKLIP with movement set to zero. Images are 1518 × 1388 mas, smoothed by an FWHM = 17 mas Gaussian (except the z' image, which has a 29 mas smoothing and pyKLIP movement = 5, and a deeper stretch). North is up, and east is left in these, and all following, images.

good correction at Hα even on faint $I \sim 10$ mag guide stars in median $\sim 0\overset{''}{.}65$ seeing conditions (whereas, a laser guide star WFS system could not deliver better correction at Hα due to the cone effect; N. Siegler et al. 2007). The MagAO-X system with up to 1564 corrected modes maps to ~14 cm/actuator, making it the highest sampled AO system in the world. So, in light of all of the above design elements of MagAO-X, deeper, much more sensitive, surveys for Hα planets are finally possible.

2.3. Introduction to TYC 5709-354-1 (WISPIT 2)

TYC 5709-354-1 is a 1.1 $M_{\rm Sun}$ classical T-Tauri star of age $5.1^{+2.4}_{-1.3}$ Myr (Letter 1), which is actively accreting. It was discovered by the WISPIT survey and VLT/SPHERE H-band imaging to have a spectacularly large cavity with two bright outer rings and a dark gap centered at ~68 au followed by another bright ring (Letter 1). At a nearby distance of just 133 pc (GAIA; L. Lindegren et al. 2021; see discussion in Letter 1) with its complex ring system and its young age, TYC 5709-354-1 (henceforth WISPIT 2) was an excellent target for MagAO-X Hα SDI imaging to determine if there were any accreting protoplanets in the central cavity or annular gaps.

3. MagAO-X Observations of WISPIT 2

3.1. The 2025 April 13 Observations of WISPIT 2

MagAO-X has a high throughput Hα SDI mode with all custom $\lambda/10$ beamsplitters (with ~95% transmission of Hα) where the Hα photons are transmitted to the two science cameras and only ~5% are lost to the wave front sensor optical path (see L. M. Close et al. 2025 for details). Moreover, this mode also allows for a very efficient SDI camera setup where another custom $\lambda/10$ beamsplitter cube transmits ~95% of the Hα continuum to a continuum filter ($\lambda_{\rm CONT}$ = 668.0 nm; $\Delta\lambda_{\rm CONT}$ = 8.0 nm) in science camera 1. This cube simultaneously reflects ~95% of the Hα light to narrowband Hα filter ($\lambda_{\rm H\alpha}$ = 656.3 nm; $\Delta\lambda_{\rm H\alpha}$ = 1.045 nm) to science camera 2. For the optical design of these two EMCCD science cameras, see the left-hand side of Figure 1 in L. M. Close et al. (2025).

For clarity and completeness, we list all of the environmental, instrumental, and reduction settings in Table A1 in Appendix A for each night WISPIT 2 was observed at Hα. Table A1 is also a summary of all of the reduction settings/values for all of our WISPIT 2 Hα observations.

On our first night (2025, April 13 UT) in slightly worse-than-average seeing ($0\overset{''}{.}68$–$1\overset{''}{.}08$), we observed WISPIT 2 for 2 hr before transit. We were able to lock the AO loop on WISPIT 2 (I = 9.9 mag) with 1000 AO modes at 1000 Hz with the gain of each mode set by MagAO-X's autogain feature. The best 64.35% of those 0.5 s integration images at Hα had an FWHM of 25 mas (Strehl = 8%–12%) and led to a 1.23 hr final integration time.

MagAO-X is particularly well suited to the discovery of Hα protoplanets due to its "photon-counting" EMCCDs. Here we set the Hα camera to near its maximum gain, so that $\mathrm{EMgain}_{\_\mathrm{H\alpha}} = 294.13 \pm 0.29$ ADU/e- (the effective readnoise = 0.05e− rms; "photon-counting" mode) in the Hα images. For the rest of the observing and instrumental setup, please see Table A1.

3.2. The 2025 April 16 Observations of WISPIT 2

Our second night of observing WISPIT 2 was better than the first night. The seeing was excellent ($0\farcs34$–$0\farcs52$), and we obtained 56 degrees of rotation (25% more than the first night). A major change was to use the 50/50 science beamsplitter cube to simultaneously observe in the z' (908 nm, BW = 131 nm) broadband continuum filter (instead of the 688 nm, BW = 8 nm Hα continuum filter). The science camera 2 remained in the Hα (656.3 nm, BW = 1.045 nm) filter, as on the previous night, but throughput was now ~50% of the maximum due to the 50/50 science cube. The AO correction was continuously excellent: we selected 99.5% of the Hα data (all of which had FWHM <24 mas), and so we had 2.16 hr of total integration (8084x 1 s frames at Hα and $32{,}336 \times 0.25$ s frames at z'). We should note that due to the selection of the 50/50 science beamsplitter and the Hα/IR WFS beamsplitter, the z' throughput was only ∼25% maximum for z'; regardless, the images were excellent, and the very high Strehl at z' made up for any throughput losses. The final Hα point-spread function (PSF) had an FWHM = 23.6 mas resolution in the 2.16 hr image (Strehl∼30%).

4. Reductions

Data reduction was with a custom pipeline (L. M. Close et al. 2025), which was designed around the fact that the flux from protoplanets at Hα is very low. Indeed, for PDS 70 b (which is similar to WISPIT 2b's Hα flux), we typically received only ∼1 Hα planet photon/pixel every 20 s—so only one in forty 0.5 s images actually detects a single Hα photon on a given planet pixel (L. M. Close et al. 2025). This implies that one needs to average 120×0.5 s exposures together before there is a good chance of ∼3 detected planet Hα photons per pixel within one FWHM-sized patch (∼4×4 pix) centered on the planet core. So binning in time (averaging) 120×0.5 s images to a 60 s average image yields ∼48 Hα photons/min from the planet's core spread over 16 pixels. This yields enough SNR for the planet signal to survive our high-pass filters and KLIP PCA PSF fitting and removal procedures on these 60 s images. Therefore, our custom python/pyIRAF pipeline (described in L. M. Close et al. 2025) was optimized for the preservation of individual photon events (each photon counted by the EMCCDs) while also maximizing the contrast with ADI and SDI (which together we call, hereafter, ASDI).

4.1. Discovery of WISPIT 2b

As described in L. M. Close et al. (2025, 2025, private communitation), the pipeline averaged the selected frames into "averaged" frames of 60 s. Then, as is usual for PCA PSF removal (J. J. Wang et al. 2015; K. B. Follette et al. 2023), these "averaged" frames were "pre-processed" to remove the low-spatial frequencies (the smooth "seeing halo") around each PSF. To do this, we high-pass filtered the images by smoothing with an FWHM = 57.3 mas Gaussian (purposely much larger than the ⩽25 mas FWHM of a planet, to preserve planet core flux) and subtracting this smoothed image from the original to remove the low-spatial frequencies, while preserving the point sources (such as planets). Unwanted flux was further removed from PSF by fitting a radial profile (centered on the core) of the images and removed from each of these frames (again, this step leaves the planet core untouched). Then, all 74x 60 s images (first night) and 130x 60 s (second night) images were fed into pyKLIP (J. J. Wang et al. 2015) to remove the PSF via PCA in the usual manner in reducing ADI data. Then, the last step is the accurate scaling of our non-coronagraphic data (multiplying the continuum by StarFlux$_{\text{\_H}\alpha}$/StarFlux$_{\text{\_CONT}}$) and subtraction of this scaled continuum image from the Hα image to yield the final ASDI image. The ASDI image should only trace true Hα emission as all residual contamination from the PSF, or scattered light off dust, should have been subtracted off (see Section 5 for more details). While we have in the past (K. B. Follette et al. 2023; J. Li et al. 2025) magnified the pixel scale of the continuum by $656.3/\lambda_{\text{CONT}}$ to exactly match the Hα diffraction rings, we skip this step here. This is because we cannot change the spatial scale of the continuum, as that shifts the positions of strong continuum emission from the dust rings, which would then poorly subtract (and actually exacerbate artifacts) at the $r \sim 200$–400 mas region of interest for these ASDI images. With WISPIT 2, we are limited more by dust structures (which rotate so pyKLIP cannot remove) than diffraction rings (which pyKLIP can mostly remove).

Once this process had been run on the 2025 April 13 data set, we discovered an SNR = 5.5 Hα emission point source near the middle of the outer annular gap of WISPIT 2 (see Figure 1, top row). This exciting discovery motivated the 2025 April 16 data set, which recovered the planet WISPIT 2b at SNR = 12.5 at Hα (see Figure 1, bottom row). There was no significant detection of continuum light (668 nm) at the location of the very cool/red planet, marking it as a very rare example of a protoplanet with Hα emission—and the first one in an annular gap. We note that the PDS 70 planets are considered to be in the large central dust-free cavity (S. Y. Haffert et al. 2019), while WISPIT 2b is outside of the central cavity, in an annular "ring" gap—sandwiched between two bright narrow dust rings, which is unique for an Hα protoplanet.

4.2. Follow-up of WISPIT 2b

Once the location of the planet was known, it was recovered in archival (2023 October 19 and 2024 October 4) H-band VLT/SPHERE IRDIS data (see Letter 1 for details). The very red protoplanet was recovered at higher SNR in deep Ks ESO-DDT images taken with VLT/SPHERE on 2025 April 26 (see Letter 1). We also obtained deep L' LBT-DDT images with the LBT with both 8.4 m apertures (unstacked, dual beam) on the LMIRcam detector, which is part of the LBTI instrument. The H and Ks images of WISPIT 2b are fully described in Letter 1. The LBT/LMIRcam L' observations are briefly described in the next section.

4.3. L′ Follow-up of WISPIT 2b at LBT

We observed WISPIT 2b at L' (3702 nm) at the LBT with the dual beam but unstacked mode of LBTI/LMIRcam (J. M. Leisenring et al. 2012; S. Ertel et al. 2020). These 2025, June 5 (UT) data were taken in subarcsecond seeing to slightly over 1″ seeing and photometric. The total amount of integration time was 3.15 hr. Only one (DX) of the 2x 8.4 m telescopes reached very high (>90%) Strehl, throughout so we just reduced the DX side (single 8.4 m scope). The L'-band data was reduced in the usual manner for nodding L' ADI (G. Weible et al. 2025). The KLIP reduced image can be seen

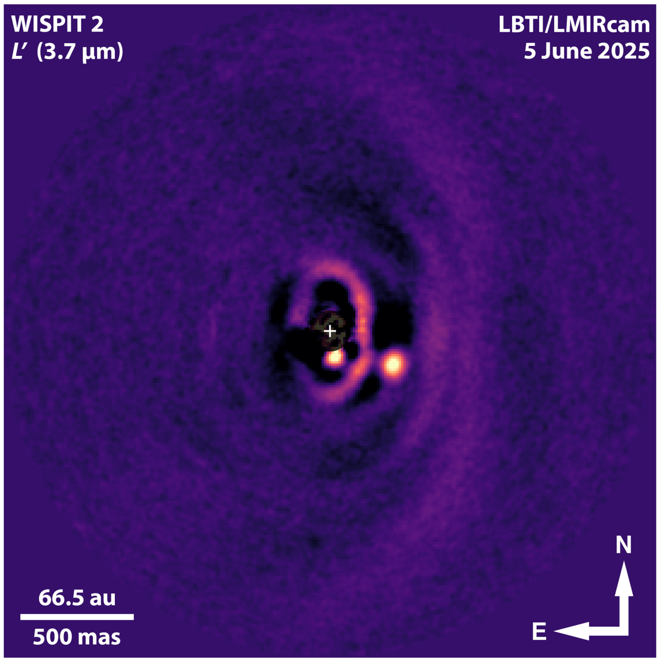

Figure 2. The KLIP reduced L' image from the LBT telescope with the LBTI LMIRcam instrument. The location of WISPIT 2b and the inner #3 and outer #2 dust rings are clear (despite the significant self-subtraction from KLIP). WISPIT 2b is located nearly in the center of the dust-free gap between the rings. The image is $1''.43 \times 1''.43$; see Appendix B for details about the L' reduction.

in Figure 2. Please see Appendix B for a complete description of all observation and reduction steps for the L' data.

5. Photometry and Astrometry

As PSF subtraction algorithms (like pyKLIP) can distort planet signal, we obtained companion astrometry and photometry through the forward modeling technique with the forward modeling feature in PyKLIP (J. J. Wang et al. 2015) for accurate measurements and uncertainties on the planet contrasts. For the astrometry, we previously observed an astrometric calibration field in Baade's Window (J. D. Long et al. 2024), which has been extensively used by MagAO and GPI. We adopt for science camera 2 (the Hα camera, used for the astrometry in this work) a platescale of $0''.00593 \pm 0''.00003$ pix^{-1}, $\mathrm{PA_{offset}} = +2.0 \pm 0.2$ deg for this work, which is almost identical to that of L. M. Close et al. (2025), which, in turn, was in excellent agreement with the VLTI/gravity orbits of PDS 70 b and c (J. J. Wang et al. 2021, 2015).

Our approach to photometry and astrometry of planet WISPIT 2b was straightforward. We used the fully forward modeled planet insertion option of pyKLIP to inject fake negative planets at the separations of b into each of the input images. Since we did not use a coronagraph for any of these observations, it is straightforward to measure the relative flux of the star and planet to obtain an accurate contrast. We fit a Gaussian to the final multi-hour "deep" WISPIT 2 A PSF core (the PSF is the median of all selected images—all linear) to find accurate subpixel stellar peak counts and planet FWHM to model the fake planets as accurately as possible in pyKLIP. This, in turn, leads to the most accurate contrasts and astrometry from pyKLIP forward modeling.

We then followed L. M. Close et al. (2025) to run a grid search to add the perfectly centered and scaled fake negative planet to completely cancel (integrated flux in planet aperture = zero) the Hα planet in the ASDI image. This yielded the $\mathrm{ASDI_{contrastH\alpha}} = (7.0 \pm 0.9) \times 10^{-4}$ on April 13 and $\mathrm{ASDI_{contrastH\alpha}} = (6.5 \pm 0.5) \times 10^{-4}$ on 2025 April 16 (see Table 1). Errors in the contrast were estimated from injecting a "ring" of six fake planets at the 309.5 mas separation and then using aperture photometry to estimate the standard deviation of planet photometry (L. M. Close et al. 2025).

We did not significantly detect any point source at SNR $\geqslant 5$ in the excellent z' data set at the location of WISPIT 2b (bottom-left panel, Figure 1). However, using a deeper stacking to 64x 120 s images (pyKLIP movement = 5) does reveal a $z' \sim 23$ mag source at $(9 \pm 5) \times 10^{-6}$ contrast at WISPIT 2b's location, but only at an SNR ~ 2. If real, this suggests a DUSTY model mass of 6 ± 2 M_{jup} (Table 2) from the z' flux. We caution that this is a very weak signal, and so this $z' \sim 23$ mag ($\Delta z' = 12.6$ mag; 9×10^{-6} contrast at 312 mas) source should not be considered a definitive detection without future confirmation. However, at Hα, the SNR > 12.5, so the planet is real.

We note the faint extended z' "arc" in between the bright ring #2 and the fainter ring #3 is due to significant pyKLIP ADI self-subtraction of the edges of the bright rings, carving negative residuals. This well-known "ringing" ADI self-subtraction of the bright disk features leads to low-spatial noise artifacts in the otherwise dark gap.

A similar forward modeling procedure was followed for the L' data sets (see Appendix B). From forward modeling (as detailed in Appendix B2), we find $\mathrm{Contrast}_{L'} = (1.76 \pm 0.07) \times 10^{-3}$. We interpolate the Wide-field Infrared Survey Explorer (WISE) absolute photometry to derive an L' flux of 8.42 ± 0.02 mag for WISPIT 2 A; hence, the magnitude of WISPIT 2b is 15.30 ± 0.05 mag, and so $ML' = 9.67 \pm 0.05$ mag. All of the L' astrometry and photometry is reported in Table 3.

6. Analysis

6.1. Example Hα Line Luminosity Calculation for WISPIT 2b 2025 April 16

The $L_{\mathrm{H\alpha}}$ luminosity can be calculated for a gap planet of an extinction corrected effective "r' mag" at Hα (which we call r' mag_p_Hα) by comparing the its flux with Vega:

$$L_{\mathrm{H\alpha}} = 4\pi D^2 f_{\mathrm{H\alpha}} = 4\pi D^2 vega_{\mathrm{zeropoint\_r'}} \Delta\lambda \{10^{\frac{r'\mathrm{mag\_p\_H\alpha}}{-2.5}}\}, \quad (1)$$

where $f_{\mathrm{H\alpha}}$ is the Hα line flux, and r'mag_p_Hα is just the effective de-extincted "r' magnitude" with respect to Vega for planet "b" at Hα.

It is then necessary to tie the photometric system from the Hα flux of WISPIT 2A (which is too variable at Hα) to the continuum flux of WISPIT 2A; so we to need calculate: $\mathrm{ASDIcontrast_{continuum}} = \mathrm{Flux_{\_H\alpha}}/\mathrm{StarFlux_{\_Cont}}$. In other words, we need to compare to the 668 nm continuum (in the r' band) since it is steady with time compared to Hα. The 4th data release of the Skymapper survey finds $r_{\mathrm{A}} = 11.09$ mag (which converts to $r'_{\mathrm{A}} = 11.07$ mag; C. A. Onken et al. 2024). We can estimate the stability of this r' flux by looking at the range of r' measurements over time: $r'_{\mathrm{A}} = 10.80$ mag (AAVSO catalog; A. Henden et al. 2016) and $r'_{\mathrm{A}} = 11.196$ mag (C. Wolf et al. 2018; additionally, $r'_{\mathrm{A}} = 11.20$ mag; Y. Huang et al. 2022). This yields a mean value of

Table 1
Discovery Hα Photometry and Astrometry for 2025 April 13 and 16 (UT) for Protoplanet WISPIT 2b

2025 Hα Data from Magellan/MagAO-X	April 13; WISPIT 2b	April 16; WISPIT 2b
Observed Hα Separation (mas)	**309.90 ± 1.60**	**309.43 ± 1.56**
Observed Hα PA (deg)	**242.71 ± 0.82**	**242.21 ± 0.41**
Forward modeled contrast results for 2b		
$\mathrm{ASDI}_{\mathrm{contrastH}\alpha}$: (flux of planet in ASDI image)/(Hα flux of star)	$\mathbf{(7.0 \pm 0.9) \times 10^{-4}}$ **(SNR = 5.5)**	$\mathbf{(6.5 \pm 0.5) \times 10^{-4}}$ **(SNR = 12.5)**
Hα line flux of planet 2b $f_{\mathrm{H}\alpha}$ (erg s^{-1} cm^{-2})	$(1.38 \pm 0.33) \times 10^{-15}$	$(1.29 \pm 0.28) \times 10^{-15}$
Planet 2b accretion rate $\dot{M}_{\mathrm{p}}$ ($Av = 0$–3 mag extinction)	$2.31^{+3.85}_{-0.21} \times 10^{-12}\ M_{\mathrm{Sun}}\ \mathrm{yr}^{-1}$	$2.25^{+3.75}_{-0.17} \times 10^{-12}\ M_{\mathrm{Sun}}\ \mathrm{yr}^{-1}$

Note. Values in bold text are directly measured; otherwise, they are calculated values.

11.06 ± 0.22 mag consistent with the 11.09 mag from the final release of Skymapper (C. A. Onken et al. 2024). Hence, we adopt for WISPIT 2 A: $r'_{\mathrm{A}} = 11.1 \pm 0.2$ mag.

To solve for $\mathrm{ASDIcontrast}_{\mathrm{continuum}}$, from our observations, as given in L. M. Close et al. (2025):

$$\mathrm{ASDIcontrast}_{\mathrm{continuum}} = \mathrm{ASDIcontrast}_{\mathrm{H}\alpha}{}^{*}\beta,$$

where, $\beta = \mathrm{StarFlux\_}_{\mathrm{H}\alpha}/\mathrm{StarFlux\_}_{\mathrm{Cont}}{}^{*}\ \mathrm{EMgain\_}_{\mathrm{CONT}}/\mathrm{EMgain\_}_{\mathrm{H}\alpha}{}^{*}\ \mathrm{QE}_{\mathrm{CONT}}/\mathrm{QE}_{\mathrm{H}\alpha}$, and where all of the parameters of β are easily measured ratios (all are listed in Table A1). The fact that β is completely dependent on ratios minimizes systematic errors that simply divide out in each ratio. Therefore, we can use the above relation to write Equation (2):

$$\begin{aligned}\Delta\mathrm{magASDI}_{\mathrm{continuum}} &= -2.5^{*} \log 10(\mathrm{ASDIcontrast}_{\mathrm{continuum}})\\ &= -2.5^{*} \log 10(\mathrm{ASDIcontrast}_{\mathrm{H}\alpha}{}^{*}\beta).\end{aligned} \tag{2}$$

Since our 2025 April 16 $\mathrm{ASDIcontrast}_{\mathrm{H}\alpha}$ is $(6.5 \pm 0.5) \times 10^{-4}$ (Table 1), and $\beta = 0.29$ (Table A1), we therefore know from Equation (2) that $\Delta\mathrm{magASDI}_{\mathrm{continuum}} = 9.31 \pm 0.12$ mag. There is also a very slight correction since there is extra ∼0.05 mag added due to Hα light in r' filter mag. So, the Hα flux projected as an "r' mag" of the planet is:

$$\begin{aligned}\mathrm{r'mag\_}p\mathrm{\_H}\alpha &= (r'_{\mathrm{A}} - A_{r'}) + (\Delta\mathrm{magASDI}_{\mathrm{continuum}} + 0.05) - A_{\mathrm{p}}\\ &= (11.1\ \pm\ 0.2 - A_{r'}) + (9.31\ \pm\ 0.12 + 0.05) - A_{\mathrm{p}}\\ &= 20.46\ \pm\ 0.32\ \mathrm{mag}.\end{aligned} \tag{3}$$

Thus, WISPIT 2b has an Hα line flux similar to an object with an r' flux 6.7×10^{-9} fainter than Vega. In the case of the slowly accreting WISPIT 2b, we have very little extinction to the star and planet (G.-D. Marleau et al. 2022) and so we will assume $A_{r'} = A_{\mathrm{p}} = 0$ (K. Wagner et al. 2018; T. Thanathibodee et al. 2019; Y. Zhou et al. 2021), so Equation (3) suggests an effective r'mag_p_Hα flux of b at Hα is similar to a continuum 668 nm ($\Delta\lambda = 8$ nm) source with an $r' \sim 20.46$ mag flux. Therefore, the line luminosity $L_{\mathrm{H}\alpha}$ can be written:

$$L_{\mathrm{H}\alpha} = 4\pi D^2 \mathrm{Vega}_{\mathrm{zeropoint\_r'}}\Delta\lambda\{10^{\frac{\mathrm{r'mag\_p\_H}\alpha}{-2.5}}\}, \tag{4}$$

which we can directly solve for in the case of WISPIT 2b as:

$$\begin{aligned}\mathrm{Log}(L_{\mathrm{H}\alpha}/L_{Sun}) &= \log{(4\pi(133 * 3.1 \times 10^{18})^2 * 2.4 \times 10^{-5}}\\ &\quad * 0.008)/[3.9 \times 10^{33} * 10^{((20.46 \pm 0.32)/2.5)}]\\ &= -6.15,\end{aligned}$$

where the Vega zero-point magnitude of the r' filter ($\mathrm{Vega}_{\mathrm{zeropoint\_}r'}$; J. Males 2013) is 2.4×10^{-5} erg/(s cm^2 μm). Since we are comparing the Hα flux to that of WISPIT 2 A in the continuum filter, we use $\Delta\lambda = 0.008\,\mu$m for our continuum filter. This $\mathrm{Log}(L_{\mathrm{H}\alpha}/L_{\mathrm{Sun}}) = -6.15$ is a significant amount of accretion emission at Hα, which allows for the very solid (SNR = 12.5) detection of the protoplanet at Hα.

To calculate the Hα line flux ($f_{\mathrm{H}\alpha}$) of b is simple, just divide the line luminosity $L_{\mathrm{H}\alpha}$ by $4\pi D^2$, as is clear from Equation (1). Therefore, the Hα line flux can be shown to be $(1.29 \pm 0.28) \times 10^{-15}$ erg s^{-1} cm^{-2} on 2025 April 16, with a full and rigorous Gaussian error analysis of Equation (4). See L. M. Close et al. (2025; their Appendix B and Figure B2) for our Gaussian error propagation technique to produce a rigorous flux error estimate. In this manner, all of the Hα line fluxes and errors in Table 1 were calculated.

In Figure 3 we plot all of the known Hα fluxes of all known Hα protoplanets with this uniform methodology. So that we can compare the different protoplanets, we normalize all of the fluxes at a distance of 113 pc (that of PDS 70). From Figure 3 we see the line flux of WISPIT 2b is very similar to all other Hα protoplanets.

6.2. Mass Accretion Calculation for WISPIT 2b

The planet mass accretion rates ($\dot{M}_{\mathrm{p}}$) were calculated as in L. M. Close et al. (2025), which used a semiempirical (E. Rigliaco et al. 2012) model of magnetospherical accretion (T. Thanathibodee et al. 2019) to estimate the mass accretion rate required for the observed line fluxes (L. M. Close 2020). We adopt here a mass of 4.9 M_{jup} consistent with the masses from Tables 2 and 3 based on the mass estimate of 4.9 M_{jup} from H and Ks planet fluxes in Letter 1 (this value is further discussed in Section 7.1 below). We adopt a radius of the planet of 1.6 R_{jup} from the DUSTY evolutionary models. In this manner, the mass accretion rates in Table 1 were calculated.

We would like to compare WISPIT 2b's $\dot{M}_{\mathrm{p}}$ values to all of the other known protoplanets. We plot these in Figure 4. Again, we see that WISPIT 2b's $\dot{M}_{\mathrm{p}}$ values are in line with those of the other protoplanets. We note that in the published version of L. M. Close et al. (2025), there was a 24x scaling error so that $\dot{M}_{\mathrm{p}}$ was too low by 24x for PDS 70 b and c. The $\dot{M}_{\mathrm{p}}$ values in this letter (in Figure 4) should be used instead for PDS 70 b and c.

7. Discussion

7.1. On the Age and Mass of WISPIT 2b

The star WISPIT 2A belongs to the young group Theia 53, which has an upper limit age of ∼13.6 Myr (Letter 1). This upper limit makes good sense for WISPIT 2 A since there is

Table 2
z' Photometry and Astrometry for 2025 April 16 (UT) for WISPIT 2b and CC1

2025 April 16: z' Data from MagAO-X	WISPIT 2b	CC1
Observed z' separation (mas)	**312 ± 5**	**109.7 ± 2.9**
Observed z' PA (deg)	**242 ± 1**	**192 ± 1**
Forward modeled contrast results from photometry Contrast$_{z'}$: (z' flux of planet)/(z' flux of star)	**$(9 \pm 5) \times 10^{-6}$ (SNR∼2)**	**$(2.4 \pm 0.5) \times 10^{-4}$ (SNR = 4.3)**
Adopted magnitude of the star WISPIT 2 A at z'	10.46 mag (C. A. Onken et al. 2024)	
Magnitude of planet at z'	∼23.1	$19.40^{+0.65}_{-0.26}$ mag
Absolute magnitude (Mz') of planet	∼17.4	$13.78^{+0.65}_{-0.26}$ mag
Est. Mass of planet from z' with DUSTY00	6 ± 2 $M_{\rm jup}$ at $5.1^{+2.4}_{-1.3}$ Myr	10 ± 1 $M_{\rm jup}$ at $5.1^{+2.4}_{-1.3}$ Myr

Note. Values in bold text are directly measured; otherwise, they are calculated values.

Table 3
L' Photometry and Astrometry for 2025, June 5 (UT) for WISPIT 2b and CC1

2025 June 5: L' Data from LBT LBTI/LMIRcam	WISPIT 2b	CC1
Observed L' separation (mas)	**315.9 ± 5.9**	**113 ± 14**
Observed L' PA (deg)	**242.16 ± 0.83**	**191.9 ± 2.4**
Forward modeled contrast results from photometry Contrast$_{L'}$: (L' flux of planet)/(L' flux of star)	**$(1.76 \pm 0.07) \times 10^{-3}$**	**$(2.80 \pm 0.37) \times 10^{-3}$**
Magnitude of the star WISPIT 2A at L'	8.42 ± 0.02 mag (WISE)	
Magnitude of planet at L'	15.30 ± 0.05 mag	$14.80^{+0.76}_{-0.43}$ mag
Absolute magnitude (ML') of planet	9.67 ± 0.05 mag	$9.18^{+0.76}_{-0.43}$ mag
Est. Mass of planet from L' with DUSTY00	5.3 ± 1.0 $M_{\rm jup}$ at $5.1^{+2.4}_{-1.3}$ Myr	8 ± 4 $M_{\rm jup}$ at $5.1^{+2.4}_{-1.3}$ Myr

Note. Values in bold text are directly measured; otherwise, they are calculated values.

still a gas rich disk around WISPIT 2. We observed Star$_{\rm H\alpha\_ph}$/Star$_{\rm CONT\_ph}$ = 0.43 (for reference, 0.125 = no Hα), which implies strong EW(Hα, 6563) = −40.5 Å in emission measured by MagAO-X on 2025 April 13. This strong stellar Hα emission implies WISPIT 2A is an actively accreting CTTS star since |EW(Hα, 6563)| > 13 Å emission, which is above the maximum expected stellar activity level for this star (D. Barrado y Navascues & E. L. Martin 2003).

We also obtained an LBT/PEPSI (K. G. Strassmeier et al. 2015) high-resolution $R \sim 250{,}000$ spectrum on 2025 June 19 (UT) and measured a lithium equivalent width of EW(Li, 6707) = 0.35 Å, indicating the strong presence of lithium and providing additional evidence that the star is indeed young and consistent with membership in Theia 53. A full analysis of the WISPIT 2A PEPSI spectra is beyond the scope of this letter and will be presented elsewhere. Our measured lithium and Hα strength, in concert with other arguments (see Letter 1), allow us to adopt an age of $5.1^{+2.4}_{-1.3}$ Myr for WISPIT 2.

From our adopted $5.1^{+2.4}_{-1.3}$ Myr age range, we find a mass range for the planet 5.3 ± 1.0 $M_{\rm jup}$ from the DUSTY evolutionary models (I. Baraffe et al. 2002) applied to our L' photometry in Table 3. This is consistent with the WISPIT 2b mass of $4.9^{+0.9}_{-0.6}$ $M_{\rm jup}$ found from H and Ks photometry in Letter 1. It is worth noting that the age of the planet could be younger than the star, and so these masses could be considered an upper limits. On the other hand, the age of any one star is very hard to definitely measure, so ages/masses could be higher than our estimate. However, as part of Theia 53, it must be less than ∼13.6 Myr (Letter 1). So even in the extreme oldest case of 13.6 Myr, it yields a DUSTY model L' mass ∼9.5 $M_{\rm jup}$; hence, the planet's mass is still within the planetary mass regime even at this old age. We may also be slightly (∼10%) overestimating the mass of the planet from the L' flux alone. The slightly higher $M_{\rm p} = 5.3 \pm 1.0$ $M_{\rm jup}$ mass derived at L' is 0.4 $M_{\rm jup}$ higher compared to that estimated at H and Ks (Letter 1) might be due to a bit of excess L' light from a warm CPD dust component warmed by the planet itself. But the fact that the L', H, and Ks model masses are all very consistent within the errors ($\Delta M_{\rm p} = 0.4^{+1.5}_{-1.3}$ $M_{\rm jup}$) suggests that the CPD thermal L' emission is a relatively minor component of the L' light from WISPIT 2b, and so most of the L' light is likely from the planet's photosphere.

7.2. Are Some Inclinations Preferred for the Detection of Hα Protoplanets?

While for many years the only bona fide Hα protoplanets were PDS 70 b and c, we now have the addition of MaXProtoPlanet 1b (J. Li et al. 2025) and WISPIT 2b, so now is a good time to look at this small, but important, exoplanet population. The first Hα protoplanet detection was LkCa 15b (S. Sallum et al. 2015), where later, the sparse aperture masking continuum "detections" of LkCa 15 b, c, and d were shown to be, in fact, tracking dust clumps in the inner disk (T. Currie et al. 2019). However, the SNR = 6 Hα detection of LkCa 15b still seems robust, and there have been recently other (L. M. Close et al. 2025, private communication) Hα detections; so in this section, we will also consider LkCa 15b as an Hα protoplanet candidate.

It is interesting to note that the inclinations of these Atacama Large Millimeter/submillimeter Array (ALMA) disks in continuum are 37°, 44°.0, 50°.1, and 51°.7 (MaXProtoPlanetS 1b; WISPIT 2b; LkCa 15b; PDS 70 b and c, respectively; see Figure 3). This group is heavily clumped $37° \leqslant i \leqslant 52°$ and is a priori unlikely to be selected from a random drawing of four inclinations from 0°–90°. However, the sample size is small, and this could be just a strange coincidence, or a consequence

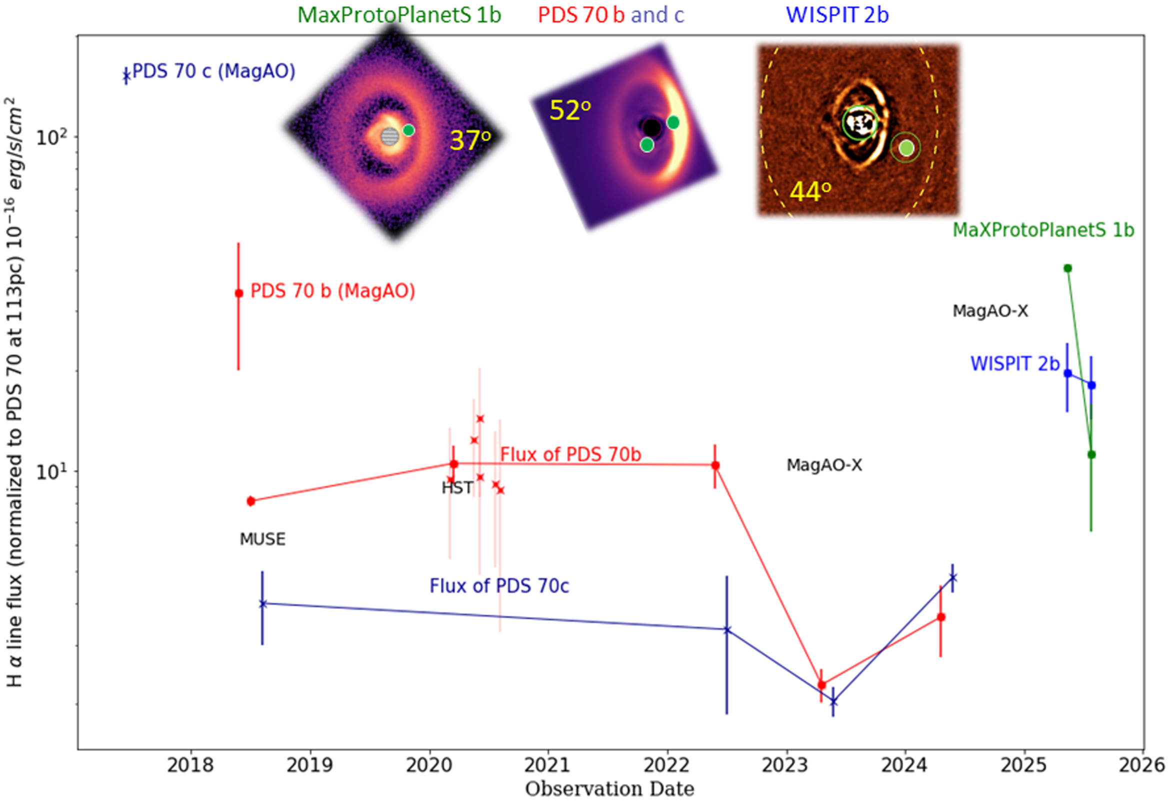

Figure 3. The calculated Hα line fluxes of all known Hα protoplanets, assuming no extinction ($A_R = A_p = 0$ mag). They have been normalized to 113 pc (the distance to PDS 70). This covers 8 yr of observations and covers all known Hα observations from the literature. We include rotated and scaled thumbnail insets in scattered light of each of the systems with well-known Hα protoplanets. The green circles each represent the location of the Hα planet in that system. While the sample to date is very small, notice how all of these systems have similar inclinations. Note how the full day side of these protoplanets is never seen. Inset disk images: MaXProtoPlanetS 1's disk in polarized scattered light from C. Ginski et al. (2025); PDS 70's disk in polarized light from Z. Wahhaj et al. (2024); and WISPIT 2's disk in z' from this work. Inclinations fit to the Atacama Large Millimeter/submillimeter Array (ALMA) continuum disk images are called out in yellow text on insets.

of selection effects in the parent population of transitional disks.

In Figure 5 we try to understand this parent population of ALMA large (>30 au) cavity or annular gap (>30 au) disks that have been investigated at high-contrast Hα by AO (G. Cugno et al. 2019; A. Zurlo et al. 2020; N. Huélamo et al. 2022) and/or the Hubble Space Telescope (HST; Y. Zhou et al. 2021; 2025). We see from Figure 5 that for inclinations <37°, there are 15 "detectable" planets. We define a detectable planet as a gap clearing Hα planet predicted by the MAG model (L. M. Close 2020) to have separations >115 mas (horizontal line in Figure 5) based on the observed ALMA continuum gap size. Of these 15 hypothetical planets (carving the gaps in these $i < 37°$ disks), none are detected at Hα, so the detection rate = 0/15 = 0%.

Two of these low-inclination ($i < 37°$) stars had candidate planets that were detected in the NIR (but not at Hα): AB Aur b and HD169142 b. Planet candidate HD169142 b (I. Hammond et al. 2023) is right in the cleared "ring" gap (dark annular gap between 2 dust rings), but despite deep Hα searches from MagAO, MagAO-X, and SPHERE/ZIMPOL, there has never been any Hα excess confirmed from this nearly pole-on ($i \sim 0°$) system and none from HD169142 b itself (B. Biller et al. 2014; Letter 1). Thus, we consider it a "non-Hα planet" candidate. The other low-inclination protoplanet candidate is AB Aur b, but it is not even pointlike; instead, it is an extended dusty "clump," that might be a protoplanet still embedded in its CPD, with no direct view of the Hα line formation region found after an extensive HST Hα imaging campaign (B. P. Bowler et al. 2025) and, hence, also a "non-Hα planet."

For $i > 52°$, there are five potentially detectable planets in Figure 5 (where the bias against high-inclination systems is properly considered; L. M. Close 2020). We also see from Figure 5 that none of these higher-inclination systems have Hα planets. Hence, 0/5 = 0% detection rate for $i > 52°$.

On the other hand, as is clear from Figure 5, in the range $37° \leqslant i \leqslant 52°$, we find a possible five systems with predicted planets > 115 mas. Of those five, we find Hα protoplanets around four of them (red diamonds in Figure 5), so a detection rate of 4/5 = 80%.

Only one star (HD 97048) is within this range and does not have an Hα planet. HD 97048 is at $i = 41\overset{\circ}{.}4$, but despite a ring system (C. Ginski et al. 2016; 2024) similar to WISPIT 2, it does not have a directly imaged Hα protoplanet (see N. Huélamo et al. 2022, and references within) nor any directly imaged planets. However, it has been reported that there is a planet (a few Jupiters in mass) in the outer gap, detected as an ALMA CO "velocity kink" protoplanet (C. Pinte et al. 2019), but this planet has not been directly detected at any wavelength yet.

This 80% success rate is a high rate for the direct detection of any class of exoplanets; such searches usually have planet direct detection rates of just a few percent or less. For example, the massive Gemini/GPIES survey targeted 531 stars and had only a few detections. GPIES was designed to select "blindly"

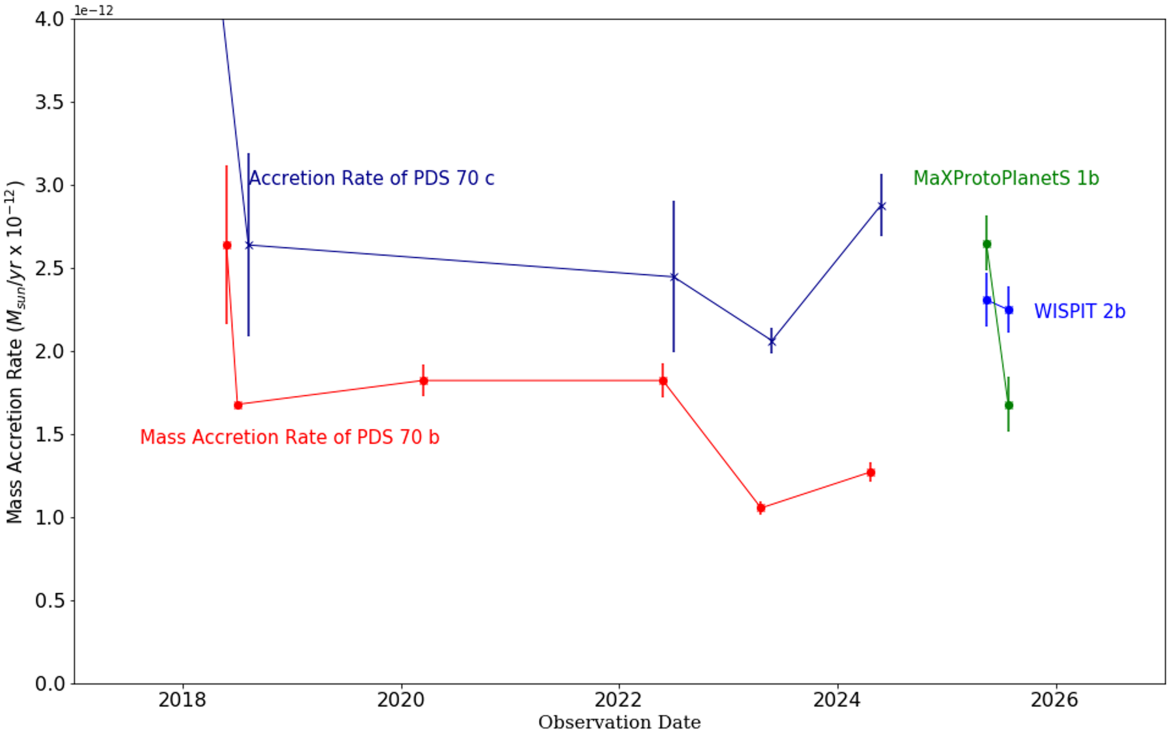

Figure 4. Similar to Figure 3 except now we plot the estimated mass accretion rates onto these planets (assuming no extinction). As can be seen, these are all currently accreting weakly ($<4 \times 10^{-12}$ $M_{\rm Sun}$ yr^{-1} or $<$0.004 $M_{\rm jup}$ Myr^{-1}). This, in turn, suggests that the Hα self-absorption by the infalling gas should be weak, and so our assumption of there being no absorption/extinction of the Hα is reasonable according to the models of G.-D. Marleau et al. (2022). We see that WISPIT 2b has a similar mass accretion rate to all of the other protoplanets. For clarity, some of the data points have been slightly shifted in time.

from a carefully selected survey of the nearby young ($\leqslant$0.5 Gyr) star population where GPIES discovered that only $9^{+5\%}_{-4\%}$ of stars have 5–13 $M_{\rm jup}$ exoplanets at 10–100 au (E. L. Nielsen et al. 2019). In contrast, we are targeting the largest (>30 au) gap transitional disks forcing these gap planets to be >115 mas separation (horizonal line in Figure 5). So it is not that surprising that we find massive (2–8 $M_{\rm jup}$), wide (20–60 au) Hα planets in the cavities and gaps of these large disks. But it is somewhat surprising that they are all (so far) in the $37° \leqslant i \leqslant 52°$ range and that 80% of our targets in this range have detected planets—and that none of the planet candidates outside this range have any Hα detected.

Our success rate does not, in any way, invalidate the exoplanet population distribution results of E. L. Nielsen et al. (2019)—wide massive exoplanets are still rare. We are just greatly improving our chances of exoplanet discovery by directly targeting wide gap transition disk stars that a priori should have "detectable" massive wide Hα planets clearing these gaps (S. Dodson-Robinson & C. Salyk 2011; L. M. Close 2020). Our work does demonstrate that Hα ASDI can be a very powerful observational technique for discovering new protoplanets in wide gaps (at least in the $37° \leqslant i \leqslant 52°$ range). Indeed, all of the well-known Hα protoplanets (PDS 70c, MaxProtoPlanetS 1b (J. Li et al. 2025), and WISPIT 2b) were all first discovered at Hα (save PDS 70 b, which was first detected at H and Ks; M. Keppler et al. 2018).

We can ask what are the a priori odds that all four Hα planets share such a clustered inclination distribution ($37° \leqslant i \leqslant 52°$) selected randomly from our "detectable" 25 large gap disks in Figure 5. In a series of 10^6 simulations of the data set of Figure 5, where we generated a similar group of 25 detectable planets (all "detectable" with separation >115 mas—separations based on the, as yet unproven, presence of gap clearing planets; S. Dodson-Robinson & C. Salyk 2011; L. M. Close 2020) and selected four randomly to be Hα planets, only 3.315% of the time did all four Hα planets cluster around any possible $\Delta i \leqslant 15°$ ranged cluster. The probability drops further to 1.076% (2.6σ) if we also impose the observed $\geqslant$80% detection rate (which means only 0 or 1 other of the 21 remaining "non-Hα planets" allowed inside the Δi range) over this cluster (as we observed in Figure 5). So, observationally speaking, inclination may appear to be important to the success at detection of Hα emission. It appears that inclinations in the range $37° \leqslant i \leqslant 52°$ are preferred. But we caution that this is still a small sample, just four Hα systems out of a possible 25 "detectable" targets, and that more Hα systems need to be found and/or searched in the future to increase (or decrease) the 2.6σ significance of this finding. Our 2.6σ significance is less than 3σ and so not yet statistically significant with this small sample size of four. In Appendix C, we speculate about one possible toy model of why the Hα produced by magnetospherical accretion onto a protoplanet might naturally be sensitive to the inclination of the line of sight.

7.3. The Search for Other Planets in the WISPIT System

Given the excellent data sets that we obtained, it is logical to carry specialized data reductions aimed at the detection of faint outer and inner planets. We carried out an extensive suite of different reductions with different pyKLIP parameters, clock induced charge mitigation, and cosmic-ray rejection algorithms, and a wide range of high-pass filters. In the end, there were no other significant (SNR > 2) Hα emission point sources found in any of our data sets. Only WISPIT 2A (the

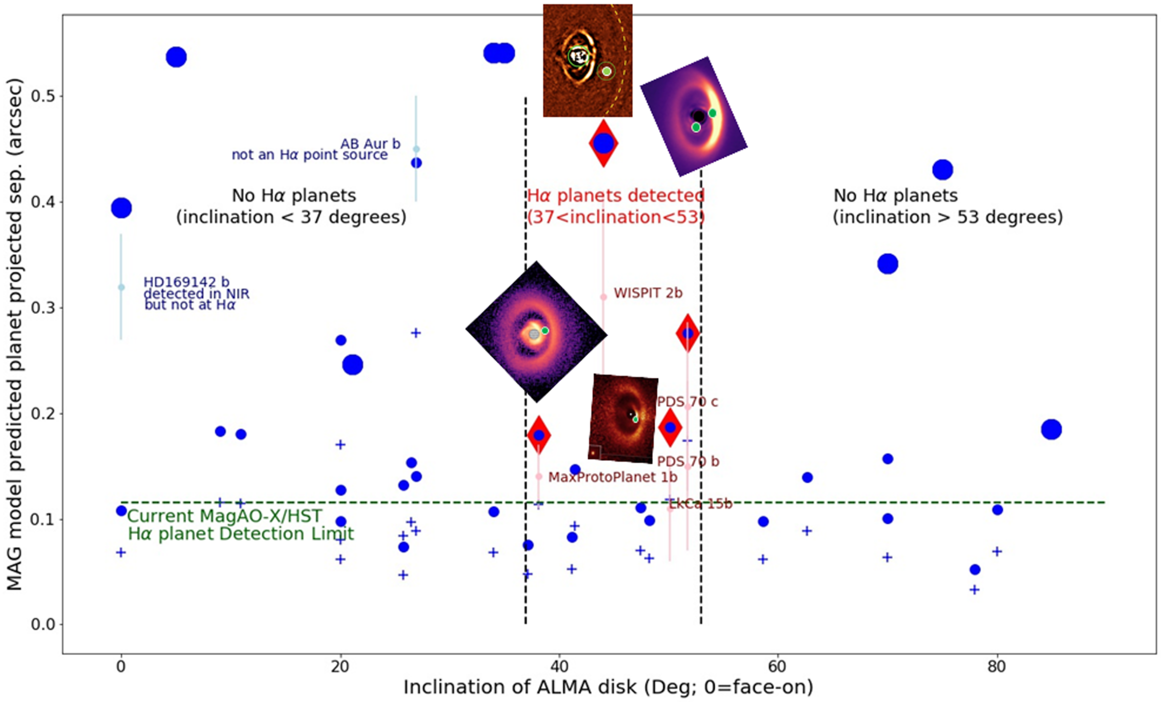

Figure 5. Here, we plot predicted planet locations for all 33 known ALMA disks that have an inner cavity or a wide gap >30 au. We use the MAG model (L. M. Close 2020) to predict the average time integrated projected separation of the massive planets that could be responsible for clearing the large gaps in all 33 of these systems. The small blue dots are the predicted locations of the outer (a_2) planet from the size of the cavity ($R_{\rm cav}$) of each ALMA disk. The small blue "+" symbols are the predicted locations of the inner planets (a_1) in 2:1 MMR with the outer planet in the cavity (L. M. Close 2020). The large blue dots are the predicted positions of the annular gap clearing planets. WISPIT 2b is the first and only known accreting Hα annular gap planet; however, the plot also shows the inclinations of the many other ring gaps (large blue dots). Note how there are, to date, only Hα planets (red diamonds) found in the zone: $37 \leq i \leq 52°$. Despite the abundance of excellent targets (any blue symbol above the green dashed line at 115 mas is considered a "detectable" Hα planet, but only those with red diamonds are actually detected), there are no Hα planets detected with inclinations <37° (pole-on systems). Nor are any found with inclinations >55°. All known protoplanets are plotted as light dots with vertical lines (these vertical error bars denote the estimated angle between the time averaged positions of the MAG model and a pole-on orbit). The red light dots are all of the known Hα protoplanets, and the blue ones are known NIR planets that seem to have no direct Hα emission.

star) and planet 2b had significant Hα emission on 2025 April 13 and 16.

7.3.1. A Close Companion: CC1

There is an intriguing inner pointlike object inside the inner cavity. In Figure 6, we show that there is a close companion candidate "CC1" (Separation = 110 mas (15 au deprojected); PA = 192°) first detected at z' (908 nm; SNR ∼ 4) with MagAO-X and then at L' (3702 nm) with LMIRcam (SNR > 12). For CC 1, we measure forward modeled point-source contrasts of $(2.4 \pm 0.5) \times 10^{-4}$ at z' ($19.40^{+0.65}_{-0.26}$ mag; Tables 2) and $(2.80 \pm 0.35) \times 10^{-3}$ at L' ($14.80^{+0.76}_{-0.43}$ mag; Table 3). In contrast to z' and L', we do not have high SNR detections of CC1 at our other NIR bands (H and Ks) likely due to the large ($d = 185$ mas) size of the (N_ALC+YJH_S) coronagraph used with SPHERE (Letter 1). Although there are hints of CC1 in total intensity (it appears unpolarized) in the 2025 April 26 "BB_Ks" SPHERE data set of Letter 1 with "ADI" and "cADI" reductions (reproduced here; bottom-left panel of Figure 6). We do not detect CC1 in the 668 nm continuum filter, nor do we have a significant Hα detection (see Figure 6, top-left panel).

7.3.2. On the Nature of CC1: A Dust Clump or an Inner Planet?

CC1 does appear slightly extended in Figure 6 at z' (but a point source at L'), so it might be a dust clump. Moreover, Figure 6 only shows a very weak Hα with a low SNR ∼ 2, and so it is likely not significant. It is not (at least on 2025 April 13 and 16) an Hα protoplanet—so it could be dust. On the other hand, it is very bright and pointlike at L', and we find CC1 has a very red color (z'–L' = 4.6 mag), which argues that CC1 could have a "warm" blackbody $T_{\rm eff} \sim 1$–2×10^3 K. The dust at 15 au is much cooler than this, and so CC1 cannot solely be produced by a passively cooling dust clump at 15 au, nor can its very red colors ($z' - L' = 4.6$ mag) be produced by starlight gray scattering off compact dust. We might be able to explain CC1 as a very special dust clump that only reflects long wavelengths (shifting the starlight to a reddened $z' - L' \sim 4.6$ mag). However, this would require very unlikely dichroic scattering dust grain properties. Indeed, the reddest known dust disk is that of HR 4796, which has an observed reflectance z'-$L' \sim 1.0$ mag/arcsec^2 (H. Zhong et al. 2024), which gives a maximum red dust color of $z' - L' \sim 2.9$ (considering the spectrum of WISPIT 2). Moreover, even the largest, reddest grains give only theoretical $z' - L'$ colors of <3.0 mag (R. Tazaki et al. 2019). Hence, our $z' - L' = 4.6$ mag color appears too red for CC1 to be solely explained by scattered light from dust. Moreover, CC1 was not detected in polarized light at Ks only detected in total intensity, also inconsistent with scattered light off dust.

Another explanation is that CC1 might possibly be a low-mass star with a dusty edge-on disk inclined directly toward our line of sight. This could produce very red colors by extinction. However, the observed smooth "non-spiral" WISPIT 2 ring system would be impossible with such a

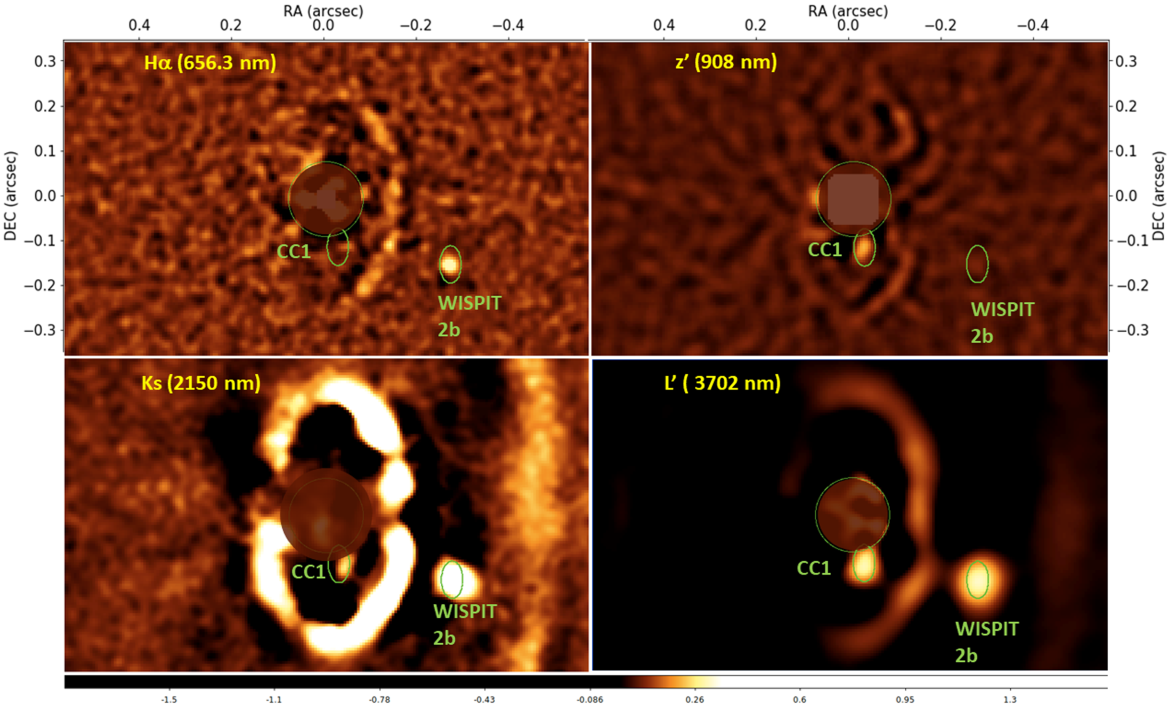

Figure 6. Here, we zoom in on the inner 1162 × 694 mas to examine the position of the close companion (CC1) at different wavelengths. The z' image is same as in Figure 1, but shown here is with movement = 0. The cADI Ks image is from SPHERE/IRDIS; see Letter 1 for details. The L' image is the same as in Figure 2, but with increased smoothing. This very red (z'–L' ∼ 4.6 mag) CC 1 source has an SNR = 4.3 in the z' image and SNR = 12.1 in the L' image. There is little difference between the $z' - L'$ positions (Δsep = −3 ± 14 mas and ΔPA = $0\overset{\circ}{.}1 \pm 3\overset{\circ}{.}0$), so they are consistent with being cospatial. The Ks source is partially blocked by the diffracted edge of the SPHERE r = 93 mas coronagraph (dark circle), yet is spatially consistent with the z' and L' sources within errors. CC1 is a point source at L' but appears slightly extended at z' and Ks. CC1 is not significantly detected in the Hα image (SNR < 2). The CC1 green ellipse is in the same location (110 mas; 192°) in each image. The ellipses trace $r = 41$ mas (5 au) circles with $i = 44^{\circ}$ (same as main disk). There is an $r = 83$ mas semitransparent circle centered exactly on the star. It is unclear if CC1 is a warm inner protoplanet (mass ∼9 $M_{\rm jup}$) or an unusually red compact dust clump. If it is a planet, it could appear modesty extended due to its dusty CPD's edge scattering starlight (no z' scattering occurs at 2b due to the shadow cast by ring #3). Scaling from the observed size (∼1 Hill sphere) of the PDS 70 b and c CPDs of L. M. Close et al. (2025), we predict CC1's CPD would appear elongated by $r \sim 2.7$ au. The observed size of CC1 at z' is the PSF convolved with the CPD, yielding a CPD radius of ∼24 mas at z'. Hence, CC1's CPD's edge should trace ∼60% inside of the green CC1 ellipse, roughly consistent with the elongation observed in z'.

massive inner stellar mass companion at 15 au. This is just too much tidal mass for CC1 to have so close to ring #3 and yet leave this ring completely unperturbed and symmetric.

If we look, instead, at the exoplanet hypothesis for CC1, we see the L' ($14.80^{+0.76}_{-0.43}$ mag) and z' ($19.40^{+0.65}_{-0.26}$ mag) flux of CC1 could be due to a warm dusty planetary photosphere (as is the case of WISPIT 2b). Such a hypothesis would predict that CC 1 would be an 8 ± 4 $M_{\rm jup}$ planet from its L' flux and a 10 ± 1 $M_{\rm jup}$ planet from z' flux (Tables 2 and 3; DUSTY00; I. Baraffe et al. 2002). In any case: the (1) z' and L' photometry, (2) nondetection at 668 nm, and (3) nondetection in polarized light at H+Ks are all consistent in color and magnitude with CC1 being from a photosphere of a 9 ± 4 $M_{\rm jup}$ exoplanet (DUSTY00 model). The lack of significant Hα could be due to a drop in accretion (which is known to happen to Hα protoplanets; L. M. Close et al. 2025) and/or optical extinction from its spatially extended CPD.

At a deprojected separation of 15 ± 1 au, CC 1 is consistent with the 14.4 au 8:1 MMR orbital resonance with WISPIT 2b at 57.5 au (Letter 1's orbit fit for 2b). Such an MMR could help create multiplanet orbital stability in the WISPIT 2 system (L. M. Close 2020). Moreover, the presence of a massive inner 9 $M_{\rm jup}$ planet could scatter out an outer planet, and so be the cause of having such a wide ~58 au outer 5 $M_{\rm jup}$ planet like WISPIT 2b (R. A. Smullen et al. 2016).

Future follow-up spectra at K with VLTI/gravity, or 3–4 μm with LBTI/ALES (A. J. Skemer et al. 2015), tracking orbital motion and higher-contrast coronagraphic z' and H-band imaging could all help determine if CC1 is truly another protoplanet (a "WISPIT 2c"), or an unusually red ($z' - L' \sim 4.6$ mag) compact dust clump, or perhaps a protoplanet still somewhat embedded inside its CPD.

8. Conclusions

We present nearly diffraction-limited (<25 mas) Hα images of the star TYC 5709-354-1, which was recently discovered by the WISPIT survey to have a large multi-ring transitional disk. For more details about WISPIT 2, see R. F. van Capelleveen et al. (2025), which is a companion Letter (Letter 1) to this work. Our Hα images of 2025 April 13 and April 16 discovered an accreting protoplanet. This protoplanet WISPIT 2b was at $r = 309.43 \pm 1.56$ mas (∼57.5 au deprojected assuming $i \sim 44°$ inclination coplanar orbit), PA = 242.21 ± 0.41 with a SNRs = 5.5 and 12.5, respectively. WISPIT 2b appears to be clearing a dust-free gap between the two bright dust rings in the system.

This is the first time a ring or annular gap Hα protoplanet (a protoplanet with Hα emission found between two bright and narrow dust rings; like rings #3 and #2) has been discovered. Previous Hα protoplanets (like PDS 70 b and c) have been in the large inner cavity in their star's transitional disk. Here, WISPIT 2b appears to be clearing a dust-free gap between the two bright rings of dust—as long predicted by theory.

WISPIT 2b is an actively accreting Hα protoplanet. We find Hα ASDI contrasts of $(7.0 \pm 0.9) \times 10^{-4}$ and $(6.5 \pm 0.5) \times 10^{-4}$ and so calculate an Hα line flux of $(1.38 \pm 0.33) \times 10^{-15}$ and $(1.29 \pm 0.28) \times 10^{-15}$ erg s^{-1} cm^{-2} on April 13 and 16, respectively.

We also present L' photometry from LBT/LBTI of the planet ($L' = 15.30 \pm 0.05$ mag) with the LMIRcam camera, which, when coupled with an adopted age of $5.1^{+2.4}_{-1.3}$ Myr, yields a planet mass estimate of $M_p = 5.3 \pm 1.0\ M_{\rm jup}$ and size $R_p = 1.6 \pm 0.2\ R_{\rm jup}$ from the DUSTY evolutionary models (I. Baraffe et al. 2002). Given the main parameters of the planet, we utilized the methodology of L. M. Close et al. (2025) and calculated that WISPIT 2b is accreting at $2.25^{+3.75}_{-0.17} \times 10^{-12}\ M_{\rm Sun}\,{\rm yr}^{-1}$. WISPIT 2b joins three other known Hα accreting protoplanets. WISPIT 2b is very similar to these other Hα protoplanets in terms of inferred mass (2–8 $M_{\rm jup}$), age (∼5–10 Myr), and Hα line luminosity and estimated mass accretion rates (1–3 $\times 10^{-12}\ M_{\rm Sun}\,{\rm yr}^{-1}$).

We note that the inclination of the system (44°) is very similar to all of the other known Hα protoplanet systems: $i = 37°$ (MaXProtoPlanetS 1b); 50° (LkCa 15b); and 52° (PDS 70 b and c).

We argue, despite the small sample size, that a clump of inclinations ($\Delta i \leqslant 15°$) (centered on any central value with an 80% (or higher) Hα planet detection rate) has only a 1.0% (2.6σ) probability of occurring randomly, and so we speculate that magnetospherical accretion might have preferred inclinations (37°–52°) for the direct (cloud/dust-free) line of sight to the Hα line formation/shock regions on the planetary surface. Future studies are required to see if this inclination trend is really significant. Detailed future theoretical modeling is required to see if the line of sight to Hα emission could/should be inclination dependent.

We detected a compact pointlike object CC1 in L' at 110 mas (∼15 au deprojected) at PA = 192°. We also detected CC1 at z' and Ks at this same location. CC1 has very red colors (z'–$L' \sim 4.6$ mag). It had no significant Hα emission on 2025 April 13 and 16. However, our z' and L' photometry is consistent in magnitude and color with a $9 \pm 4\ M_{\rm jup}$ exoplanet (a WISPIT 2c), or it could also be an unusually red dust clump inside the central cavity of WISPIT 2. Future observations of CC1 will be required to ascertain its true nature.

Acknowledgments

We would like to thank the anonymous referee, whose careful reading of the manuscript and excellent suggestions led to a much improved final manuscript. L.C. was partially supported by past NASA eXoplanet Research Program (XRP) grants 80NSSC18K0441 and XRP 80NSSC21K0397, which funded the MaxProtoPlanetS survey. J.L. is also supported by NSF Graduate Research Fellowship. We are very grateful for support from the NSF MRI award No. 1625441 (for MagAO-X development). The MagAO-X Phase II upgrade program is made possible by the generous support of the Heising-Simons Foundation. The results reported herein benefited from collaborations and/or information exchange within NASA's Nexus for Exoplanet System Science (NExSS) research coordination network sponsored by NASA's Science Mission Directorate. This material is based upon work supported by the National Aeronautics and Space Administration under agreement No. 80NSSC21K0593 for the program "Alien Earths."

Facilities: Magellan:Clay (MagAO-X), LBT (LBTI), LBT (PEPSI).

Software: Python (https://www.python.org/), SciPy (Virtanen et al. 2020), NumPy (Oliphant 2006), Matplotlib (Astropy Collaboration et al. 2013), astropy (Astropy Collaboration et al. 2018). The development of pyKLIP is led by Jason Wang and collaborators see https://pyklip.readthedocs.io/en/latest/. Vortex Image Processing (C. A. Gomez Gonzalez et al. 2017; V. Christiaens et al. 2023).

Appendix A
The Hα MagAO-X Observations

Table A1 is a log of all of the observations and settings for these WISPIT Hα observations.

Table A1
Log of All of the Observations, Settings, and Parameters Used for Our WISPIT 2b Hα Observations

	2025 April 13	2025 April 16
Environmental		
Seeing (")	0.″68–1.″08	0.″34–0.″52
Wind (mph)	22.7–31.4; NNE	4.9–14.6; "N"
Photometric sky?	yes	yes
Adaptive Optics Settings of MagAO-X		
Number of AO modes corrected	Auto gain 1000	Auto gain 1000
AO loop speed (Hz)	1000	1000
NCP DM	BMC 1024 (1K)	BMC 1024 (1K)
NCP aberration correction	FDPR	FDPR
EMCCD Science Camera Features		
Camera 1 filter : λ_1, $\Delta\lambda_1$ (CONT)	668.0, 8.0 nm	z' (908, 131 nm)
Camera 2 filter : λ_2, $\Delta\lambda_2$ (Hα)	656.3, 1.045 nm	656.3, 1.045 nm
Bump mask in pupil?	No, open	No, open
EM$_1$ (CONT) as set on camera 1	600	500
EM$_2$ (Hα) as set on camera 2	900	900
EMgain$_{\rm \_CONT}$ (ADU/e-)	137.52 ± 0.97	114.60 ± 0.77
EMgain$_{\rm \_H\alpha}$ (ADU/e-)	294.13 ± 0.29	294.13 ± 0.29
Readnoise$_1$ rms e- (CONT)	0.16	0.19

Table A1
(Continued)

Environmental	2025 April 13	2025 April 16
Readnoise$_2$ rms e- (Hα)	0.05	0.05
Exposure Times and WISPIT 2 Hα Observational Parameters		
Exposure time (DIT)	0.5 s	DIT$_1$ = 0.25 DIT$_2$ = 1 s
Percentage of raw frames kept	64.35%	99.5%
Number of raw Hα frames kept	8941	8084
Exposure time of combined images	120 x 0.5 = 60 s	60 x 1 = 60 s
Number of combined images fed to pyKLIP	74	130
Total deep exposure time (hr)	1.23 hr	2.16 hr
ADI sky rotation (start→stop: Δdeg)	−130→−175: 45°	−127→+177: 56°
High-pass (HP) filter value (pix)	4.1	4.1
StarFlux$_{\_\mathrm{H}\alpha}$/StarFlux$_{\_\mathrm{CONT}}$	0.624	…
QE$_{\_\mathrm{CONT}}$/QE$_{\_\mathrm{H}\alpha}$	16.8/16.6 = 1.01	NA -SciBS 50/50
r' mag of WISPIT 2A	11.1 ± 0.2	11.1 ± 0.2
FWHM of Hα PSF (deep image)	25 mas	23.6 mas
Strehl of Hα PSF (deep image)	8%–12%	30%
Beta(β) = (StarFlux$_{\_\mathrm{H}\alpha}$/StarFlux$_{\_\mathrm{Cont}}$)*(EMgain$_{\_\mathrm{CONT}}$/EMgain$_{\_\mathrm{H}\alpha}$)*(QE$_{\mathrm{CONT}}$/QE$_{\mathrm{H}\alpha}$)		
Beta (β)	0.29	0.29
SDI "contrast boost" = $1/\beta$	3.45x	3.45x
ASDIcontrast$_{\mathrm{continuum}\ =\ \mathrm{ASDIcontrastH}\alpha}$ * β = (ASDI planet flux)/(star continuum flux)	$b = (2.0 \pm 0.2) \times 10^{-4}$	$b = (1.8 \pm 0.1) \times 10^{-4}$
pyKLIP parameters and SNR		
pyKLIP sectors, annuli, PC modes	4, 10, 5	4, 10, 5
pyKLIP movement	0	0
SNR of b in ASDI image	5.5	12.5

Appendix B
LBTI/LMIRcam L' Data Reduction

B1. L$'$ Observations and Reductions

TYC 5709-534-1 was observed with the Large Binocular Telescope Interferometer (LBTI: P. M. Hinz et al. 2016; S. Ertel et al. 2020) and the L/M-band InfraRed Camera (LMIRcam: M. F. Skrutskie et al. 2010; J. M. Leisenring et al. 2012) with an L' filter (λcen = 3.702 μm, $\Delta\lambda$FWHM = 0.584 μm) on 2025 June 5. The observations used the (pupil-stabilized) double-sided direct imaging mode with wave front correction provided by the adaptive secondary mirrors of the LBT AO "SOUL" system (S. Esposito et al. 2010; V. Bailey et al. 2014; E. Pinna et al. 2016, 2023). The telescope was nodded in an ABAB pattern for modeling and subtraction of the background. Five nondestructive reads were collected "up the ramp" for each 2540.97 ms exposure, alternating nod positions every 250 exposures out of 5000 for a total exposure time of ~3.53 hr >62° of field rotation, enabling ADI-based PSF subtraction (C. Marois et al. 2006).

A custom IDL+Python pipeline adapted from that described in G. Weible et al. (2025) was used for preprocessing; the following corrections are applied to each exposure. We performed a linear fit to the ramps after excluding saturated values. Poor fits ($r^2 < 0.8$) and negative slopes were masked. Standard calibrations (dark-subtraction, flat-fielding) were applied, and a bad-pixel mask was generated from the calibration frames. Bad pixels were interpolated with the nearest 24 good values. Vertical and horizontal striping was removed by subtracting the median of each column and row from itself after masking the stellar PSFs, and we iteratively sigma-clipped the images with 3–7 pixel 3.5σ filters. A PCA-based subtraction of the thermal background was employed following S. Hunziker et al. (2018) and H. Rousseau et al. (2024), with the 1000 nearest frames taken at the alternate position used as references. We retained the top 10 PCs from the eigen decompositions and masked the target frames' PSFs before projection. These projection coefficients were used to reconstruct the complete background models from the unmasked eigenimages. The frames were de-striped a second time in the same manner as before and corrected for optical distortion from a warping solution provided by pinhole-grid observations (A. L. Maire et al. 2015; E. Spalding & J. Stone 2019). Note that 331 × 331 subarrays centered on the PSF locations were cropped for post-processing.

The AO correction for the DX (right) pupil was found to attain a significantly higher Strehl ratio than that of the SX (left). The following processing is applied only to the DX images to prioritize recovering signals close to the diffraction limit of $\lambda/D \approx 90$ mas. The stellar PSFs were centered to subpixel precision with 2D Gaussian fits using the *cube_recenter_2dfit* vortex image processing (VIP; C. A. Gomez Gonzalez et al. 2017; V. Christiaens et al. 2023) Python function. Centered images were separated into two semi-independent data sets for separate processing: one for each nod position. The inner regions of the frames of each data set were correlated with their temporal median, and the ~10% of images having the lowest Pearson correlation coefficients were trimmed with the *cube_detect_badfr_correlation* VIP function. The 4457 retained images (effective exposure ~3.15 hr) were centered a second time with 2D Gaussian fits. Residual background offsets measured in an annulus were subtracted, and each stellar PSF was normalized to its mean flux.

B2. KLIP and Forward Modeling L' *Photometry and Astrometry*

For our primary (forward modeling) reduction, the images were binned temporally by 1 (3) with a mean. We use the pca annular VIP implementation of the KLIP algorithm with a parallactic angle (PA) threshold to model and subtract the stellar PSFs (A. Amara & S. P. Quanz 2012; R. Soummer et al. 2012; O. Absil et al. 2013). We reduce only the inner $\sim 1\overset{\prime\prime}{.}49$ ($\sim$640 mas) of each frame for the primary (forward modeling) reduction. The PA constraint for PSF references corresponds to an arclength $\approx$1 FWHM for planet b. We retain the top nine PCs for subtraction and combine the residual images with an inverse-variance weighted trimmed mean (T. D. Brandt et al. 2013; M. Bottom et al. 2017). The reduced images from the two nodding positions were averaged. The result from our primary reduction is shown north-up in Figures 2 and 6 with a platescale of $10.624^{+0.035}_{-0.038}$ mas pixel^{-1}, as determined from routine astrometric observations of the Orion Trapezium.

Relative astrometry and L' photometry of planet b and CC1 are found from iterative injections of scaled Gaussian PSF models into the two semi-independent data sets before PSF subtraction and combination. We used the *firstguess* VIP function to minimize the standard deviation of residuals in an FWHM-diameter aperture at the location of the point source. For ease of computation, the forward modeled residual images are median-combined. The forward modeling results are presented in Table 3. Uncertainties were computed as detailed in G. Weible et al. (2025), except that the standard deviations of aperture photometry and 2D Gaussian centroids for a given source (b, CC1) and two corresponding artificial injections at rotated PAs, i.e., of six measurements per source including both nod positions, were used to estimate measurement uncertainties.

Appendix C

Why Inclination Might Matter for the Observability of Hα

The heating effect of magnetospherical accretion on the upper cloud layers of protoplanets is an interesting topic that has not been extensively studied. While Z. Zhu et al. (2016), Y. Aoyama et al. (2018), T. Thanathibodee et al. (2019), Y. Aoyama et al. (2021), and G.-D. Marleau et al. (2022) all extensively study the accretion process itself, the convective heating effect on the protoplanet's upper atmospheric clouds is usually ignored.

In Figure C1 we show a cartoon of a toy model where infalling (free-falling) hydrogen gas (thin blue arrows) impacts on the upper atmosphere of a protoplanet. The heating in the Zel'dovich shock temperature spike ($\Delta T_{\rm shock} \sim 8000$ K) would reasonably drive strong convection into the upper atmosphere of the planet. The buoyancy from such a $\Delta T_{\rm shock}$ would not be too dissimilar to that of the Shoemaker–Levy 9 impactors on Jupiter (H. B. Hammel et al. 1995). Using those observed convective plume heights ($\sim$5% of $R_{\rm jup}$) as a guide, it is possible that "steady-state" cloud plumes of $\sim$1%–10% of the planet radius ($R_{\rm p}$ $\sim$1.6 $R_{\rm jup}$) could occur. Absorption from these opacity sources (especially true of these dusty atmospheres where dust is well mixed in the upper atmosphere; I. Baraffe et al. 2002) along our line of slight to the Hα shock can explain the puzzling lack of Hα planets found with inclinations $<37^\circ$ or $>52^\circ$ (see Figure 5). It also helps explains how, on the other hand, $\sim$80% of ALMA disks that have $37^\circ \leqslant i \leqslant 52^\circ$ and gap widths $>$30 au are detected to have Hα protoplanets (like WISPIT 2b). This is because, at these angles, we are looking straight down the accretion flow—with a direct line of slight to the Hα line formation region on the protoplanet (Figure C1).

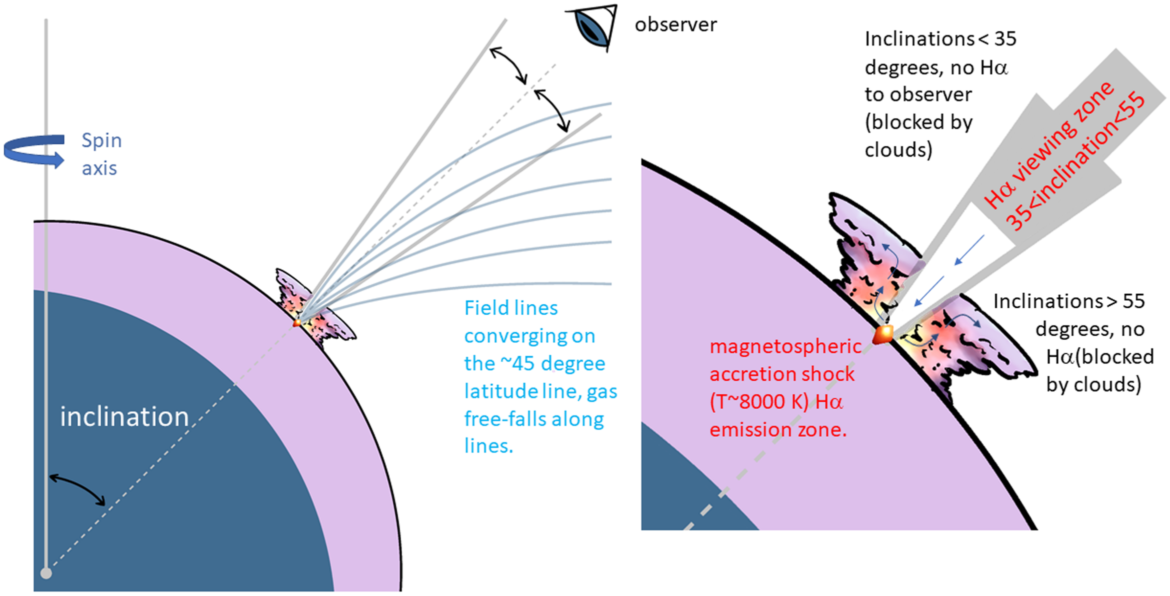

Figure C1. A simple cartoon to show how the Hα line formation zone from magnetospheric accretion could be best viewed by looking straight down the magnetic field lines (G.-D. Marleau et al. 2022). In other words, an observer would have the most direct line of sight to the Hα line formation zone if the ALMA disk and its coplanar planet were both inclined at the line of latitude of where the magnetic field lines (drawn here fixed at 45°). Here, we show a toy model where the heating in the Zel'dovich shock temperature spike ($\Delta T_{\rm shock}$) would reasonably drive strong convection in the dusty atmosphere of the planet. The buoyancy from such a $\Delta T_{\rm shock}$ would not be dissimilar to that of the Shoemaker–Levy 9 impactors on Jupiter and lead to the quasi-static $\sim$5% $R_{\rm p}$ dusty cloud deck heights shown here.

We caution that this is just a concept, and other concepts are also possible and certainly may prove to be more likely. This toy model is presented here to start the discussion about inclination. Moreover, this model requires a rigorous theoretical modeling effort that properly accounts for the accretion heating, cloud formation/growth and radiative transfer through the opacity sources—but that is beyond the scope of this Letter.

ORCID iDs

Laird M. Close https://orcid.org/0000-0002-2167-8246
Richelle F. van Capelleveen https://orcid.org/0009-0002-6729-646X
Gabriel Weible https://orcid.org/0000-0001-8009-8383
Kevin Wagner https://orcid.org/0000-0002-4309-6343
Sebastiaan Y. Haffert https://orcid.org/0000-0001-5130-9153
Jared R. Males https://orcid.org/0000-0002-2346-3441
Matthew A. Kenworthy https://orcid.org/0000-0002-7064-8270
Jialin Li https://orcid.org/0000-0002-8110-7226
Joseph D. Long https://orcid.org/0000-0003-1905-9443
Christian Ginski https://orcid.org/0000-0002-4438-1971
Alycia J. Weinberger https://orcid.org/0000-0001-6654-7859
Kate Follette https://orcid.org/0000-0002-7821-0695
Joshua Liberman https://orcid.org/0000-0002-4934-3042
Katie Twitchell https://orcid.org/0009-0002-9752-2114
Jay Kueny https://orcid.org/0000-0001-8531-038X
Daniel Apai https://orcid.org/0000-0003-3714-5855
Rene Doyon https://orcid.org/0000-0001-5485-4675
Kyle Van Gorkom https://orcid.org/0000-0002-4877-7762
Olivier Guyon https://orcid.org/0000-0002-1097-9908
Maggie Y. Kautz https://orcid.org/0000-0003-3253-2952
Eden McEwen https://orcid.org/0000-0003-0843-5140
Ya-Lin Wu https://orcid.org/0000-0002-4392-1446
Jacob Isbell https://orcid.org/0000-0002-1272-6322
Emmeline Close https://orcid.org/0009-0008-7611-3999
Elena Tonucci https://orcid.org/0009-0006-4370-822X
Matthijs Mars https://orcid.org/0000-0001-7353-3391

References

Absil, O., Milli, J., Mawet, D., et al. 2013, A&A, 559, L12
Amara, A., & Quanz, S. P. 2012, MNRAS, 427, 948
Aoyama, Y., Ikoma, M., & Tanigawa, T. 2018, ApJ, 866, 84
Astropy Collaboration, Price-Whelan, A. M., Sipőcz, B. M., et al. 2018, AJ, 156, 223
Astropy Collaboration, Robitaille, T. P., Tollerud, E. J., et al. 2013, A&A, 558, A33
Aoyama, Y., Marleau, G.-D., Ikoma, M., & Mordasini, C. 2021, ApJL, 917, L30
Bailey, V., Hinz, P., Vaitheeswaran, V., et al. 2014, in Exploring the Formation and Evolution of Planetary Systems, 299, ed. M. Booth, B. C. Matthews, & J. R. Graham (Cambridge: Cambridge Univ. Press), 26
Baraffe, I., Chabrier, G., Allard, F., & Hauschildt, P. H. 2002, A&A, 382, 563
Barrado y Navascues, D., & Martin, E. L. 2003, AJ, 126, 2997
Biller, B., Males, J., Rodigas, T. J., et al. 2014, ApJL, 792, L22
Bowler, B. P., Zhou, Y., Biddle, L. I., et al. 2025, AJ, 169, 258
Bottom, M., Ruane, G., & Mawet, D. 2017, RAAS, 1, 30
Brandt, T. D., McElwain, M. W., Turner, E. L., et al. 2013, ApJ, 764, 183
Christiaens, V., Gonzalez, C., Farkas, R., et al. 2023, JOSS, 8, 4774
Close, L. M. 2020, AJ, 160, 221
Close, L. M., Follette, K. B., Males, J. R., et al. 2014, ApJL, 781, L30
Close, L. M., Males, J. R., Durney, O., et al. 2018, Proc. SPIE, 10703, 107034Y
Close, L. M., Males, J. R., Li, J., et al. 2025, AJ, 169, 35
Cugno, G., Quanz, S. P., Hunziker, S., et al. 2019, A&A, 622, 156
Currie, T., Marois, C., Cieza, L., et al. 2019, ApJL, 877, L3
Demars, D., Bonnefoy, M., Dougados, C., et al. 2023, A&A, 676, A123
Dodson-Robinson, S., & Salyk, C. 2011, ApJ, 738, 131
Ertel, S., Hinz, P. M., Stone, J. M., et al. 2020, Proc. SPIE, 11446, 1144607
Espaillat, C., Calvet, N., D'Alessio, P., et al. 2011, ApJ, 728, 49
Esposito, S., Riccardi, A., Fini, L., et al. 2010, Proc. SPIE, 7736, 773609
Follette, K. B., Close, L., M., Males, J., R., et al. 2023, AJ, 165, 225
Francis, L., & van der Marel, N. 2020, ApJ, 892, 111
Ginski, C., Pinilla, P., Benisty, M., et al. 2025, A&A, 699, A237
Ginski, C., Stolker, T., Pinilla, P., et al. 2016, A&A, 595, A112
Gomez Gonzalez, C. A., Wertz, O., Absil, O., et al. 2017, AJ, 154, 7
Haffert, S. Y., Bohn, A. J., de Boer, J., et al. 2019, NatAs, 3, 749
Hammel, H. B., Beebe, R. F., Ingersoll, A. P., et al. 1995, Sci, 267, 1288
Hammond, I., Christiaens, V., Price, D. J., et al. 2023, MNRAS Letters, 522, L51
Henden, A., Templeton, M., Terrell, D., et al. 2016, yCat, 2336, 0
Hinz, P. M., Defr'ere, D., Skemer, A., et al. 2016, Proc. SPIE, 9907, 990704
Huang, Y., Yuan, H., Li, C., et al. 2022, ApJ, 924, 141
Hunziker, S., Quanz, S. P., Amara, A., & Meyer, M. R. 2018, A&A, 611, A23
Huélamo, N., Chauvin, G., Mendigutía, I., et al. 2022, A&A, 668, A138
Keppler, M., Benisty, M., Müller, A., Henning, T., et al. 2018, A&A, 617, A44
Kueny, J., Van Gorkom, K., Kautz, M., et al. 2024, arXiv:2407.13019
Leisenring, J. M., Skrutskie, M. F., Hinz, P. M., et al. 2012, Proc. SPIE, 8446, 84464F
Lindegren, L., Bastian, U., U. Biermann, M., et al. 2021, A&A, 649, A4
Li, J., Close, L. M., Long, F., et al. 2025, ApJL, in Press
Long, J. D., Pearce, L., Haffert, S. Y., et al. 2024, AJ, 169, 36
Males, J. 2013, PhD thesis, The Univ. Arizona
Males, J. R., Close, L. M., Haffert, S. Y., et al. 2022, Proc. SPIE, 12185, 1218509
Males, J. R., Close, L. M., Haffert, S. Y., et al. 2024, arXiv:2407.13007
Males, J. R., Close, L. M., Miller, K., et al. 2018, Proc. SPIE, 10703, 1070309
Maire, A. L., Skemer, A. J., Hinz, P. M., et al. 2015, A&A, 576, A133
Marleau, G.-D., Aoyama, Y., Kuiper, R., et al. 2022, A&A, 657, A38
Marois, C., Lafreni'ere, D., Doyon, R., Macintosh, B., & Nadeau, D. 2006, ApJ, 641, 556
Nielsen, E. L., De Rosa, R. J., Macintosh, B., et al. 2019, AJ, 158, 13
Onken, C. A., Wolf, C., Bessell, M. S., et al. 2024, PASA, 41, e061
Oliphant, T. E. 2006, A guide to NumPy, Vol. 1, (Trelgol Publishing USA)
Pinna, E., Esposito, S., Hinz, P., et al. 2016, Proc. SPIE, 9909, 99093V
Pinna, E., Rossi, F., Agapito, G., et al. 2023, in Adaptive Optics for Extremely Large Telescopes (AO4ELT7), 80
Pinte, C., van der Plas, G., Ménard, F., et al. 2019, NatAs, 3, 1109
Rigliaco, E., Natta, A., Testi, L., et al. 2012, A&A, 548, A56
Rousseau, H., Ertel, S., Defr'ere, D., Faramaz, V., & Wagner, K. 2024, A&A, 687, A147
Sallum, S., Follette, K. B., Eisner, J. A., et al. 2015, Natur, 527, 342
Siegler, N., Close, L. M., Burgasser, A. J., et al. 2007, AJ, 133, 2320
Skemer, A. J., Hinz, P., & Montoya, M. 2015, Proc. SPIE, 9605, 96051D
Skrutskie, M. F., Jones, T., Hinz, P., et al. 2010, Proc. SPIE, 7735, 77353H
Smullen, R. A., Kratter, K. M., & Shannon, A. 2016, MNRAS, 461, 1288
Soummer, R., Pueyo, L., & Larkin, J. 2012, ApJL, 755, L28
Spalding, E., & Stone, J. 2019, Dewarp: Distortion Removal and On-sky Orientation Solution for LBTI Detectors, Astrophysics Source Code Library, ascl:1907.008
Strassmeier, K. G., Ilyin, I., Järvinen, A., et al. 2015, AN, 336, 324
Szulágyi, J., Binkert, F., & Surville, C. 2022, ApJ, 924, 1
Szulágyi, J., & Mordasini, C. 2017, MNRAS letters, 465, L64
Tazaki, R., Tanaka, H., Muto, T., Kataoka, A., & Okuzumi, S. 2019, MNRAS, 485, 4951
Thanathibodee, T., Calvet, N., Bae, J., Muzerolle, J., et al. 2019, ApJ, 885, 94
van Capelleveen, R. F., Ginski, C., Kenworthy, M. A., et al. 2025, ApJL, 8, L8
Van Gorkom, K., Males, Jared, R., Close, Laird, M., et al. 2021, JATIS, 7, 039001
Virtanen, P., Gommers, R.., Oliphant, T. E., et al. 2020, Nat Methods, 17, 261
Wahhaj, Z., Benisty, M., Ginski, C., et al. 2024, A&A, 687, A257
Wagner, K., Follete, Katherine, B., Close, Laird, M., et al. 2018, ApJL, 863, L8
Wang, J. J., Ruffio, J.-B., De Rosa, R. J., et al. 2015, pyKLIP: PSF Subtraction for Exoplanets and Disks, Astrophysics Source Code Library, ascl:1506.001
Wang, J. J., Vigan, A., Lacour, S., et al. 2021, AJ, 161, 148
Weible, G., Wagner, K., Stone, J., et al. 2025, AJ, 169, 197
Wolf, C., Onken, C. A., Luvaul, L. C., et al. 2018, PASA, 35, e010
Zhu, Z., Ju, W., & Stone, J. M. 2016, ApJ, 832, 193
Zhong, H., Ren, B., Ma, B., et al. 2024, A&A, 64, A168
Zhou, Y., Bowler, B. P., Sanghi, A., et al. 2025, ApJL, 980, L39
Zhou, Y., Bowler, B. P., Wagner, K. R., et al. 2021, AJ, 161, 244
Zurlo, A., Cugno, G., Montesinos, M., et al. 2020, A&A, 633, 119